RSC Advances

REVIEW

View Article Online
View Journal | View Issue

Cite this: *RSC Adv.*, 2025, **15**, 33561

Silicon-based anodes for solid-state batteries: challenges, opportunities, and multiscale strategies

Zhenjun Zhang, Xiangyong Xue,* Zuxue Mo, Xiaoxu Lei, Xuerui Xie, Haiqing Qin, Yilong Wu, Haowen Jiang and Huijie Tang

Received 17th July 2025
Accepted 2nd September 2025

DOI: 10.1039/d5ra05126f

rsc.li/rsc-advances

Solid-state batteries (SSBs) have become a hot topic in next-generation energy storage research due to their high safety and potential high energy density. Si has a high theoretical specific capacity (4200 mAh g^{-1}), moderate lithium insertion potential (0.4 V *vs.* Li^+/Li), and abundant resources, making it a subject of significant interest. However, its application is limited by factors such as significant volume expansion (>300%), interface dynamic instability, and slow reaction kinetics. In this work, the key challenges and opportunities of silicon-based anodes in SSBs are systematically reviewed. A multi-level synergistic design strategy is proposed, encompassing material alloying, nano-structuring, composite structure design, and optimization of electrode and electrolyte compatibility. Furthermore, prospects for future scientific research and commercialization of high-performance silicon-based SSBs are presented.

1 Introduction

Lithium-ion batteries (LIBs) are widely used in 3C electronic products, electric vehicles, and large-scale energy storage due to their high operating voltage, high energy density, low self-discharge, no memory effect, and excellent cycle performance.[1] However, existing LIB technology has nearly reached its theoretical limits in terms of volumetric energy density and weight-based capacity, making it difficult to meet the growing market demand.[2] Additionally, safety concerns associated with LIBs during charging and discharging limit their further application in energy storage. Therefore, solid-state batteries (SSBs) with high energy density, high safety, and a wide operating temperature range are considered a key research focus for next-generation battery systems, capable of effectively addressing these issues. SSBs are poised for rapid development, with emerging technologies including SSBs featuring graphite anodes, lithium-free SSBs (for example, Zn, Mg, Ga, and Al systems), metal–air batteries, and 3D-printed SSBs. Leveraging the intrinsic advantages of solid-state electrolytes (non-flammability and low self-discharge), these technologies exhibit tremendous potential in simplifying system management and enhancing safety, thus emerging as crucial directions in next-generation energy storage.[3]

One critical pathway to boost SSB performance lies in developing high-capacity electrode materials. Fig. 1a shows that a typical SSB comprises a cathode, solid-state electrolyte (SSE), and anode. The anode material selection is particularly crucial for enhancing battery energy density (Table 1). Lithium metal (Li), with its ultrahigh theoretical capacity (3862 mAh g^{-1}) and the lowest redox potential (0 V *vs.* Li^+/Li),[4] is considered the ultimate anode material. Yet its practical implementation faces significant limitations (Fig. 1b–d), including severe Li dendrite growth,[5,6] void formation, interfacial instability, decomposition of sulfide SSEs at Li interfaces,[7] low critical current density (CCD),[8] and stringent operational requirements.[9] Of particular concern is Li dendrite penetration through SSE separators, which may cause internal short circuits and pose substantial safety hazards.

In the landscape of materials, silicon (Si) and germanium (Ge) exhibit remarkable advantages (Table 1). They feature higher melting points (Si: 1410 °C; Ge: 938.2 °C) than metallic lithium and lower reactivity with organic electrolytes, endowing batteries with superior cycling stability and safety while effectively suppressing lithium dendrite growth during charge–discharge processes.[10] Notably, Si boasts high theoretical specific capacities of 3579 mAh g^{-1} (based on the $Li_{15}Si_4$ phase) and 4200 mAh g^{-1} (based on the $Li_{22}Si_4$ phase).[11,12] Its moderate lithiation potential not only avoids the dendrite risks associated with metallic lithium deposition but also significantly enhances the battery energy density through its high capacity. Moreover, Si's abundance in the Earth's crust (27.7%), low cost, and environmental friendliness make it a highly promising anode candidate for SSBs.

Currently, many studies have been reported on silicon-based anodes in SSBs. Deng *et al.*[13] proposed modification strategies for silicon-based materials, such as morphology control, amorphization, and compositing. Zhao *et al.*[14] reported strategies including silicon-based material design, compositing, and

---

Guangxi Key Laboratory of Superhard Material, National Engineering Research Center for Special Mineral Materials, Guangxi Technology Innovation Center for Special Mineral Materials, China Nonferrous Metals (Guilin) Geology and Mining Co., Ltd, Guilin 541004, PR China. E-mail: 179430756@qq.com

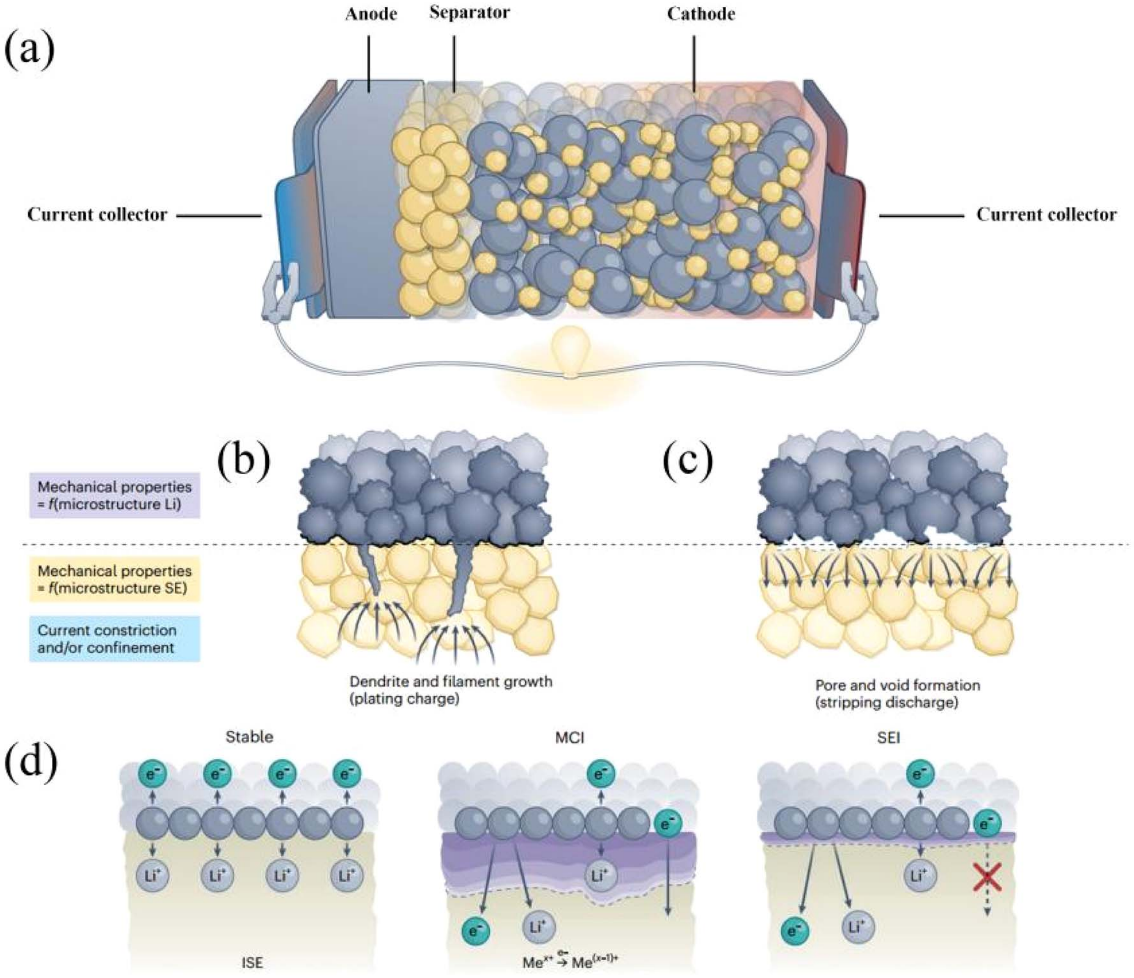

Fig. 1 (a) Schematic illustration of a typical solid-state lithium battery structure.[16] Disadvantages associated with lithium anodes: (b) growth of lithium dendrites and filaments; (c) regeneration of lithium dendrites; (d) interfacial behaviors between lithium metal and different SSEs: thermodynamically stable (for example, garnet-type oxide electrolytes, left), kinetically unstable (middle), and kinetically stable (right). MCI: mixed conducting interphase. ISE: inorganic solid electrolyte.

Table 1 Comparison of parameters for different anode materials (all capacity values are for the delithiated state except for lithium metal)

Materials	Li	Al	Si	Sn	Ge	Sb	C	Ti	Mg
Density (g cm^{-3})	0.53	2.7	2.3	7.3	5.32	6.7	2.25	4.51	1.3
Lithiated phase	Li	LiAl	$Li_{4.4}Si$	$Li_{4.4}Sn$	$Li_{4.4}Ge$	Li_3Sb	LiC_6	$Li_{4.4}Ti_5O_{12}$	Li_3Mg
Theoretical specific capacity (mAh g^{-1})	3862	993	4200	996	1600	660	372	175	3350
Volume change (%)	100	93	420	260	180	200	12	5	100
Potential *versus* Li (V)	0	0.3	0.4	0.6	0.4	0.9	0.05	1.5	0.1

alloying, while analyzing interfacial issues and electrochemical–mechanical coupling effects. Song *et al.*[15] investigated prelithiation, SEI formation mechanisms, and large-scale production from multiple perspectives, including materials, electrodes, and battery packaging. However, the optimization strategies in these reports are mostly focused on single-level modification of silicon materials (for example, nanosizing and composite design), with less involvement in the application of novel binders and current collector modification. Moreover, existing reports mainly focus on sulfide systems, lacking a comparative analysis of other SSEs. In this work, the mechanism of silicon-based anodes in SSBs is reviewed, and the key challenges and opportunities they face are deeply analyzed. Based on this, the research progress on improving the performance of silicon-based anodes through multi-dimensional strategies such as alloying, nanosizing, material composite, application of novel binders, modification of current collectors, and electrolyte optimization (including the matching of sulfide, oxide, polymer, and composite solid electrolytes) is emphatically discussed, providing a theoretical basis for the development of high-performance silicon-based SSBs.

2 Challenges for Si anodes

Si is regarded as an ideal candidate for next-generation high-energy-density LIBs due to its wide applicability, high theoretical lithium storage capacity (4200 mAh g^{-1}), and low lithiation potential (~0.4 V *vs.* Li^+/Li). However, several critical challenges still hinder its practical implementation. The failure mechanisms of silicon-based materials are shown in Fig. 2.

2.1 Electrode loss

On one hand, Si particles undergo extrusion and fragmentation during cycling. Fig. 2a shows the significant volume changes of Si particles during Li-ion insertion/extraction generate substantial internal stresses. These stresses cause the Si particles to be squeezed and fragmented, leading to the loss of electrical contact between numerous Si particles and their neighboring units, conductive networks, and current collectors. This loss of electrical contact severely impairs the electrochemical performance of the electrode, hindering efficient electron transport within the electrode structure and ultimately resulting in the attenuation of overall battery capacity. It has been reported that Si particles have a critical diameter of approximately 150 nm.[18] When the particle diameter is less than 150 nm, Si particles neither crack nor pulverize. For particles with a diameter larger than 150 nm, during the first lithiation process, the movement of the two-phase interface (crystalline Si core/amorphous Li–Si alloy shell) generates tensile hoop stress in the surface layer, initiating surface cracks. Subsequent cycles of Li^+ insertion/extraction will promote further propagation of these cracks, ultimately leading to particle fracture (pulverization). Atomic force microscopy (AFM) studies further confirm that microcracks form on the Si surface during delithiation, exacerbating structural degradation.[2] On the other hand, Si electrodes exhibit significant morphological and volumetric changes at the macroscale. As shown in Fig. 2b, the severe volume effects induce cracking in the electrode structure and detachment of active materials from the current collector. The detached active materials lose their electrical connection and cannot participate in subsequent electrochemical reactions, leading to the loss of their Li storage capacity.

2.2 Interface instability

Fig. 2c shows that the interfacial stability issues of silicon-based anode materials are primarily reflected in the dynamic evolution process of the SEI film. According to reports, characterization techniques such as high-resolution transmission electron microscopy (HRTEM), Fourier-transform infrared spectroscopy (FTIR), and X-ray photoelectron spectroscopy (XPS) have confirmed that the SEI film formed on the surface of silicon-based anodes mainly consists of inorganic components (Li_2CO_3, LiF, Li_2O) and organic components (various lithium alkyl carbonates and non-conductive polymers). This composite-structured SEI film exhibits typical compositional characteristics found in conventional anode materials.[19–21]

However, the significant volume expansion/shrinkage of up to 300–400% during the charge–discharge cycles of silicon-based anodes poses a severe challenge to the stability of the SEI film.[22] During lithiation, silicon particles expand, and during delithiation, they contract. This periodic volume change causes the SEI layer formed in the expanded state to crack during the contraction phase, exposing fresh Si surfaces to the

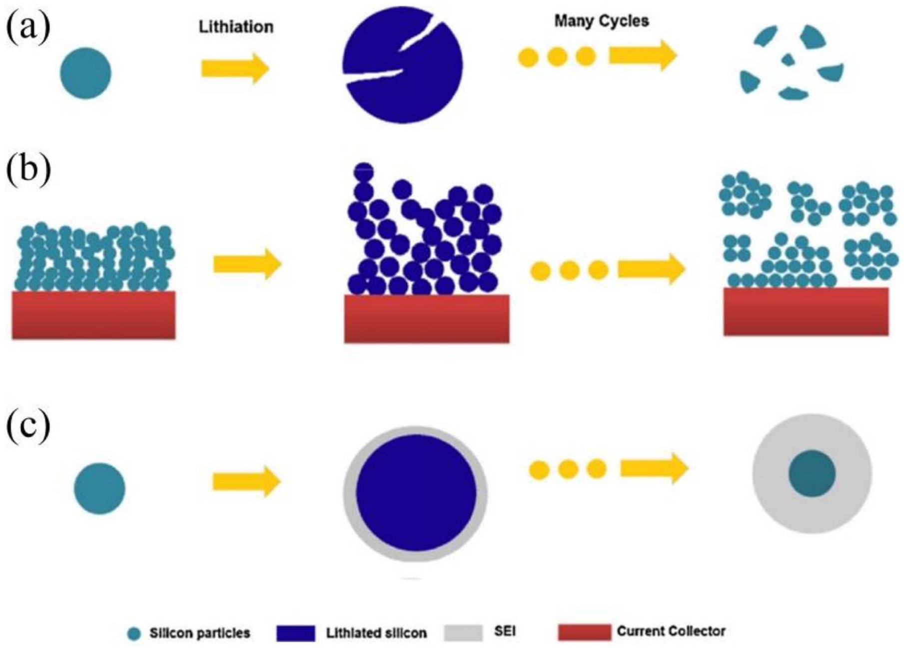

Fig. 2 Failure mechanisms of Si:[2,17] (a) extrusion and pulverization; (b) electrode detachment; (c) SEI evolution.

electrolyte and triggering repeated SEI regeneration.[23] This volume-change-induced continuous rupture-regeneration mechanism of the SEI leads to the continuous thickening of the interfacial layer during cycling, which has become a major obstacle restricting the application of silicon-based materials in liquid electrolyte lithium-ion batteries (LELIBs). The thickened SEI layer increases the lithium-ion transport impedance and continuously consumes the active lithium inventory, resulting in a significant decline in the electrochemical performance and cycle life of the battery.[24] This phenomenon is particularly prominent in LELIBs, severely limiting the practical application potential of silicon-based materials.

In addition, the inherently low electrical conductivity of silicon materials (10^{-5}–10^{-3} S cm^{-1} at 25 °C) further exacerbates the interfacial issues.[25] During the ion insertion/extraction process, the insufficient conductivity limits the electron transport efficiency, leading to increased electrode polarization. The increased polarization further affects the charge–discharge performance of the battery, reduces the fast charge–discharge capability, and consequently lowers the overall energy efficiency, which hinders the practical application of silicon-based anodes.

2.3 Slow reaction kinetics

In addition to the challenges of unstable SEI films and significant volume expansion, the inherently sluggish reaction kinetics of silicon anode materials severely limit their electrochemical performance.[26] Unlike typical intercalation-type anodes such as graphite and $Li_4Ti_5O_{12}$, the lithium storage mechanism in silicon involves the breaking of Si–Si covalent bonds and the formation of Li–Si ionic bonds. This conversion reaction process requires a high energy barrier, leading to pronounced potential hysteresis and significantly reducing the energy efficiency of the battery. Studies have shown that the diffusion kinetics of lithium ions in silicon-based materials present a significant bottleneck, with the diffusion coefficient of Li^+ in the silicon matrix being only 10^{-13}–10^{-12} cm^2 s^{-1},[27] far lower than that of spherical graphite (10^{-10}–10^{-9} cm^2 s^{-1}).[28] This slow ionic diffusion results in substantial concentration polarization during charge and discharge processes, particularly under high-rate conditions.[29] Therefore, kinetic optimization of silicon-based anodes should focus on enhancing electrical conductivity and ionic diffusion capabilities.[30–33] In addition, although Si has a high theoretical capacity, its bulk density and actual volume capacity are low, which further limits its practical application.[34] To effectively address this issue, researchers have proposed many strategies, including size control, material and interface engineering, and process optimization.[35–37]

3 Opportunities of Si anodes in solid-state electrolytes

Silicon-based materials exhibit more promising prospects in SSBs compared to LELIBs, primarily in the following aspects:

3.1 Mechanical support of solid-state electrolytes

In LELIBs, the volumetric expansion of silicon-based anode materials during charge–discharge cycles leads to electrode structure degradation and loss of electrical contact. In contrast, the rigid structure of SSEs can effectively constrain the volume expansion of silicon particles, reducing inter-particle mechanical stress and maintaining electrode structural integrity.[38] Zhang *et al.*[39] fabricated a $Li_{21}Si_5$/Si–$Li_{21}Si_5$ dual-layer composite anode with a three-dimensional conductive network *via* cold-press sintering. Benefiting from the mechanical confinement of the SSE, this anode exhibited only 14.5% volume expansion after 1000 cycles at a current density of 2.5 mA cm^{-2}, significantly lower than its performance in liquid electrolyte systems. More importantly, the rigid framework of SSEs effectively suppresses particle pulverization during cycling. Even when the silicon particle surface is uniformly lithiated, the maximum internal stress can be controlled at approximately 20 GPa. The high mechanical modulus of SSEs greatly reduces the risks of particle pulverization, detachment, and consequent conductive network breakdown, providing a critical foundation for achieving long-cycle stability of Si anodes in SSBs.

3.2 Interface stabilization

Another central challenge of Si anode electrodes in LELIBs is the dynamic and unstable solid–liquid interface problem, which the solid–solid interfacial properties of these SSBs are effectively improved:

3.2.1 Stabilization of the SEI layer. In LELIBs, the substantial volume changes of Si anodes cause repeated rupture and regeneration of the SEI layer (Fig. 3a), leading to continuous irreversible consumption of active lithium and escalating interfacial impedance. In SSBs, this issue is mitigated by the solid–solid contact mode. Xu *et al.*[23] reported that even after Si particle volume changes, SSEs do not flow like liquid electrolytes to cover newly exposed Si surfaces. Fig. 3b shows that this characteristic avoids continuous thickening of the SEI layer due to repeated exposure to fresh Si surfaces, effectively preventing additional SEI formation and enabling higher capacity retention in SSBs. Bok *et al.*[40] confirmed this improvement. After 100 cycles at 0.05C, the Si anode with liquid electrolyte exhibited a capacity retention of only 53.3% and a capacity of 800 mAh g^{-1}, whereas the Si anode using a gel polymer electrolyte showed higher capacity retention (79.4%) and a higher capacity of 1191 mAh g^{-1}. This indicates that suppressing excessive SEI growth in SSBs is crucial for enhancing capacity and capacity retention.

3.2.2 Enhanced interface stability. Liquid electrolytes are prone to continuous side reactions (for example, electrolyte decomposition) at the interface with Si, which are further exacerbated by the volume expansion of Si.[41] In contrast, many solid electrolyte materials exhibit wider electrochemical stability windows with silicon anodes, enabling the formation of chemically more stable interfaces. More importantly, certain solid electrolytes (for example, sulfides and polymer composites) can form self-healing interfaces with Si to some extent, accommodating volume changes.[42] This more stable interface not only reduces interfacial resistance but also significantly

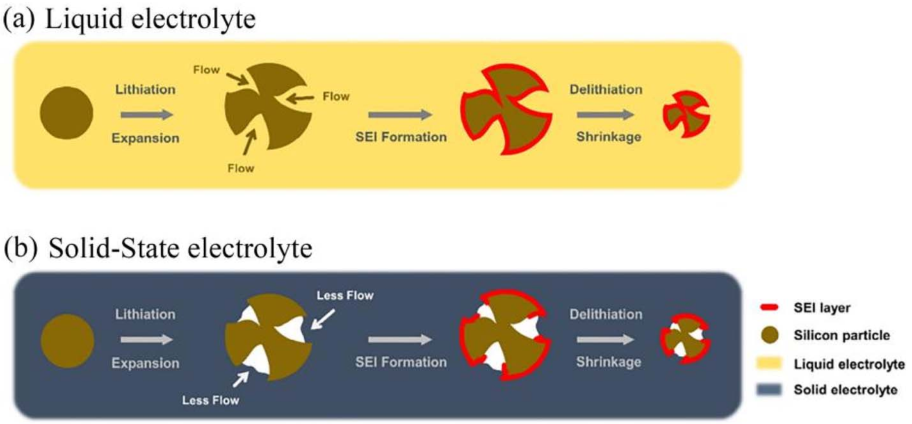

Fig. 3 The formation process of SEI in Si anodes:[10] (a) liquid electrolyte; (b) solid-state electrolyte.

improves long-cycle stability. For instance, a study pairing a garnet-type solid electrolyte ($Li_7La_3Zr_2O_{12}$) with a silicon-based anode reported retention of 2700 mAh g^{-1} initial capacity after 100 cycles, attributed to the formation of a relatively stable interface.[43]

3.3 Enhancement of areal capacity and energy density

The intrinsic safety advantages of SSBs (no leakage, non-flammable) eliminate the limitations associated with liquid electrolytes, offering greater flexibility in electrode design. In SSBs, there is no need to reserve a large amount of space for liquid electrolytes or address the side reactions they cause. Therefore, a higher proportion of high-capacity silicon-based active materials can be effectively integrated into the anode structure. Tan *et al.*[44] utilized the interfacial passivation properties of sulfide solid electrolytes to achieve a loading mass of 99.9% for Si-based anodes. This enables the ultra-high theoretical specific capacity of Si to be more fully utilized in SSBs architecture, thereby achieving higher energy density.

4 Material design strategies

To effectively address the challenges facing silicon-based materials, researchers have proposed a variety of solutions (Table 2 lists optimization strategies with typical examples). These strategies aim to overcome the limitations of Si, such as its significant volume expansion during lithiation, low electrical conductivity, and the formation of an unstable SEI layer, thereby enhancing the performance and commercial feasibility of silicon-based anodes in SSBs.

4.1 Alloying

Alloying Si with other metals is a promising approach to improve its electrochemical performance. Studies have shown that metallic elements such as Fe, Cu, and Ti can form metal silicides with Si, which can significantly enhance the electrical conductivity of silicon-based materials and accelerate electron transfer. According to the properties of metals, the metallic elements used for silicon alloying can be roughly divided into two categories: active metals and inactive metals. Common active metal–silicon alloys include Si–Mg, Si–Al, and Si–Fe, inactive metal–silicon alloys include Si–Ti, Si–Ni, and Si–Cu.[45] Moreover, since these alloying metals themselves possess lithium storage capabilities, they can synergistically contribute to the capacity, forming high-capacity composite materials.[46,47] It is worth noting that Cu is introduced into the silicon-based anode as an active composite component at this point. When Cu acts as a current collector, due to differences in the crystal

Table 2 Optimization strategies for silicon-based anodes

Strategies		Typical examples				ICE	Ref.
		Anode	Electrolyte	Current	Cycling performance		
Alloying		Mg_2Si	Li_6PS_5Cl	0.3 A g^{-1}	Over 300 mAh g^{-1} (300 cycles)	—	49
Nano-structuring	Solid nanowires	Si NWs@SSFC	$LiPF_6$	0.2C	826.3 mAh g^{-1} (500 cycles)	68.6%	56
	Hollow nanotube	DWSiNTs	$LiPF_6$	10C	Approximately 600 mAh g^{-1} (6000 cycles)	76%	57
	Nanospheres	MPSS	$LiPF_6$	0.5C	Over 1500 mAh g^{-1} (500 cycles)	—	58
	Porous nano morphology	SiMg5.0	$75Li_2\cdot 25P_2S_5$	0.026C	1038 mAh g^{-1} (200 cycles)	71%	59
Composite structure design		μSi/SWCNT	Li_6PS_5Cl	1C	1271 mAh g^{-1} (400 cycles)	85.4% (0.1C)	60
New binder (GA)		Si	$LiPF_6$	1C	2000 mAh g^{-1} (500 cycles)	88.1% (0.1C)	61
Current collector optimization		CuSi	$LiPF_6$	C/12	850 mAh g^{-1} (30 cycles)	76%	62

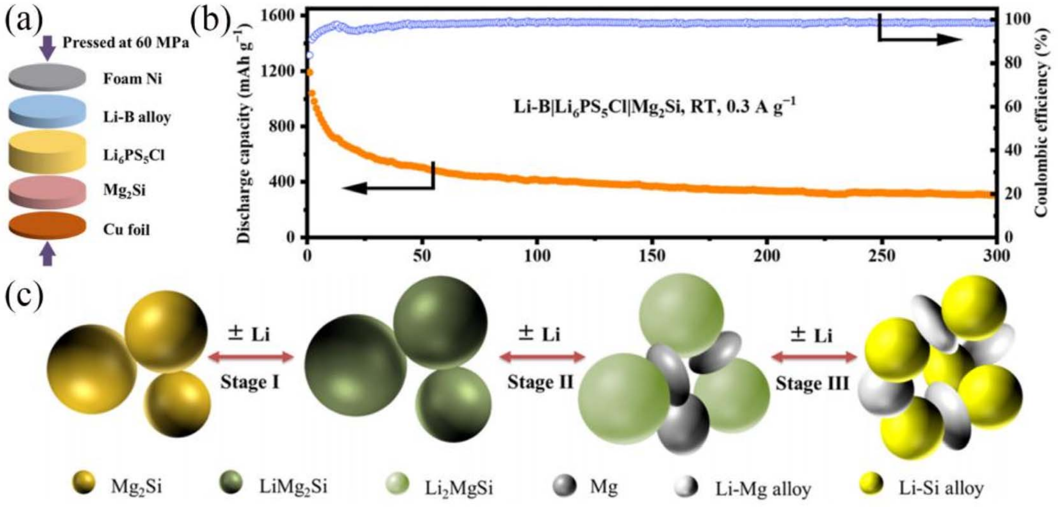

Fig. 4 (a) Layer-by-layer stacking process of the Mg_2Si battery; (b) cycling performance at a current rate of 0.3 A g^{-1}; (c) schematic illustration of the charging/discharging processes of Mg_2Si.

lattice and atomic radius between Cu and Li, it forms a solid solution rather than an alloy with Li, and only plays a role in conductivity and support.[48] In addition, the addition of metallic materials endows the silicon surface with good mechanical strength, which can release the stress generated by volume expansion during cycling and maintain electrochemical stability.

In the SSEs, the Mg_2Si electrode designed by Cai *et al.*[49] demonstrated excellent comprehensive performance. Fig. 4a shows that the battery was fabricated using a layer-by-layer stacking process. When matched with the Li_6PS_5Cl sulfide solid-state electrolyte, this Mg_2Si electrode exhibited an electronic conductivity as high as 8.9×10^{-2} S cm^{-1}, an ionic conductivity of 9.7×10^{-5} S cm^{-1}, and a lithium-ion diffusion coefficient ranging from 0.14 to 9.18×10^{-11} cm^2 s^{-1}. As depicted in Fig. 4b, at a current density of 0.3 A g^{-1}, the Mg_2Si electrode achieved a discharge capacity of 1190.7 mAh g^{-1}, a reversible charge capacity of 994.8 mAh g^{-1}, and an initial coulombic efficiency (ICE) of 83.5%. Fig. 4c further illustrates the structural evolution process of Mg_2Si during the conversion reaction. Its performance stems from a unique reversible crystalline phase reconstruction mechanism, which ensures the stability of the mixed conductive network throughout the entire lifespan of the electrode, thereby enabling rapid electrode reaction kinetics. Compared with traditional composite electrodes, the Mg_2Si electrode significantly reduces interfacial side reactions caused by inactive components. This structural design provides new insights for the practical application of silicon-based SSBs.

4.2 Nano-structuring

It can be concluded from the above that crystalline Si will not fracture when its particle size is smaller than the critical value (150 nm). This is because the strain energy stored by the electrochemical reaction is insufficient to overcome the resistance of surface energy, thereby inhibiting the propagation of cracks and keeping the particles intact.[50] However, the critical value of amorphous Si is approximately 870 nm, which is higher than that of crystalline Si. The reasons are as follows:[51,52] (1) the concentration of Li in the formed lithiated phase is lower, resulting in a smaller volume expansion amplitude compared to crystalline Si. (2) Amorphous Si is an isotropic material, which avoids the stress concentration caused by the anisotropic expansion of crystalline Si. (3) The reaction front may be thicker, alleviating the accumulation of stress. These factors together contribute to the larger critical value of amorphous Si than that of crystalline Si. This indicates that size regulation (nanonization) can mitigate the loss caused by the volume effect of Si and improve the lithiation degree of Si anodes. Meanwhile, the nanoscale dimension shortens the Li$^+$ diffusion path, further improving the electrochemical performance.

Although the application of stack pressure can effectively address some issues of silicon-based materials, optimizing the nanostructure design remains a crucial strategy for enhancing the performance of SSBs.[13] Li *et al.*[53] systematically investigated the influence of Si particle size on the electrochemical performance by constructing SSBs consisting of $LiNi_{0.8}Mn_{0.1}Co_{0.1}O_2$ (NMC811)/$Li_{10}Si_{0.3}PS_{6.7}Cl_{1.8}$ (LSPSCl)/Si–X. Their results further confirmed that nano-silicon exhibits more advantages than micro-silicon in SSBs. The cycling processes of micro-silicon (>1 μm) and nano-silicon are shown in Fig. 5, respectively. Under the same high stack pressure, the larger Si particles in micro-silicon (>1 μm) are limited by lithium chemical reactions and diffusion, achieving only partial lithiation and forming unlithiated cores.[54,55] In contrast, nano-silicon is more completely lithiated during the lithiation process, and the silicon particles do not undergo fracture or pulverization. Moreover, even after prolonged charge–discharge cycles, nano-silicon still maintains good interfacial contact without the growth of lithium dendrites.

4.2.1 Solid nanowires. Among various silicon nanostructures, Si nanowires (Si NWs) represent a further advancement, as they not only possess the general advantages of

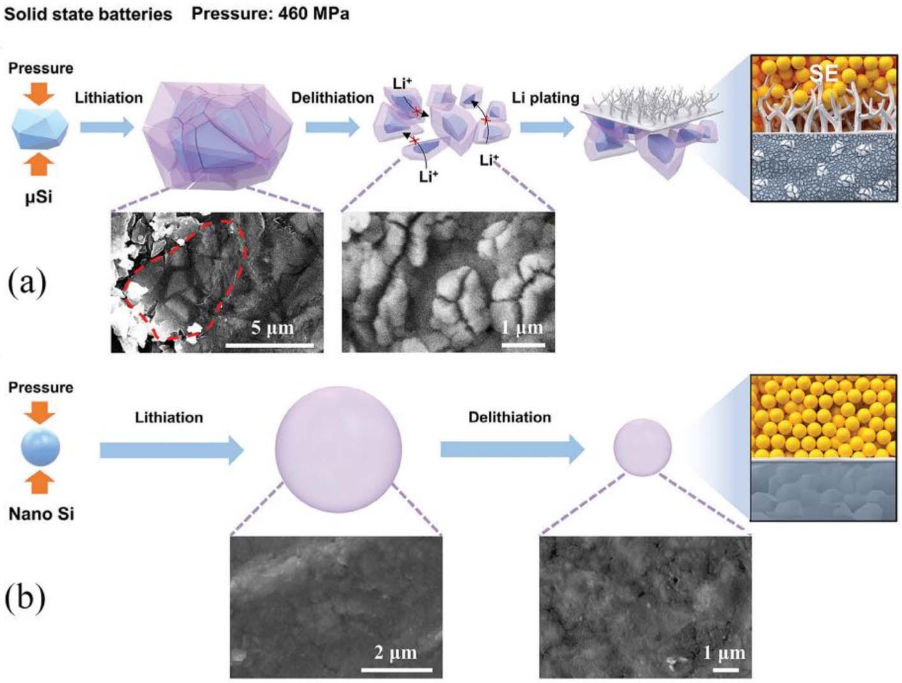

Fig. 5 Schematic illustration of the size effect during the charge–discharge process of batteries with Si anodes of different dimensions: (a) micro-silicon; (b) nano-silicon.

nanomaterials (notably strain resistance) but can also be directly grown on and connected to current collectors, thereby eliminating the need for additional binders and conductive carbon-based materials.[63]

Nguyen *et al.*[63] proposed a strategy for growing Si NWs in a plasma-enhanced chemical vapor deposition (PECVD) reactor. Fig. 6a–c show the SEM images of Si NWs with a high interconnection rate and a schematic diagram of the interconnection effect. This structure effectively prevents individual nanowires from detaching from the substrate due to excessive strain at the root during lithiation, exhibiting excellent structural stability and electrochemical performance. The Si NWs maintained almost 100% capacity retention after 40 cycles at 0.5C, with a capacity of approximately 3100 mAh g^{-1}. Moreover, the capacity retention remained 90% after 70 cycles at 2C. Cui *et al.*[64] reported a core–shell nanowire structure with a crystalline Si core and an amorphous Si shell, grown on a stainless steel substrate *via* a simple one-step synthesis method. Its crystalline Si core can serve as a stable mechanical support and an effective conductive channel, while the amorphous shell can store Li^+.

Imtiaz *et al.*[56] designed a facile method for directly growing Si NWs on a stainless steel fiber cloth (SSFC) substrate (Fig. 6d). Fig. 6e and f show the scanning electron microscopy (SEM) morphology of the Si NWs@SSFC composite and the transmission electron microscopy (TEM) structure of a single Sn-seeded Si NW, respectively. The unique network structure of this composite has dual advantages: on one hand, it provides high-density loading sites for catalyst seeds; on the other hand, it offers buffer space for the inherent significant volume expansion and contraction of Si during lithiation/delithiation cycles. This unique structure enables the Si NW loading to exceed 1.3 mAh cm^{-2}, which can significantly improve the areal capacity and energy density of the electrode. The material exhibits excellent rate performance (Fig. 6g). At a high rate of up to 5C, samples with loadings of 1.03 mg cm^{-2} and 1.32 mg cm^{-2} can still deliver specific capacities of 254 mAh g^{-1} and 184.6 mAh g^{-1}, respectively. In terms of areal capacity (Fig. 6h), the electrode with a loading of 1.32 mg cm^{-2} achieves a high reversible areal capacity of 3.03 mAh cm^{-2} at 0.1C. In addition, the material also shows excellent cycling stability. As shown in Fig. 6i, a high specific capacity of 1221.1 mAh g^{-1} is still retained after 500 cycles. Even at a high mass loading of up to 1.32 mg cm^{-2}, the electrode can still provide a specific capacity of 826.3 mAh g^{-1}.

4.2.2 Hollow nanotube.

Hollow Si nanotubes (H-SiNTs) offer an effective buffer against the substantial volume expansion inherent in silicon-based materials during charge–discharge cycles, owing to their unique hollow structure. This configuration not only optimizes Li^+ transport pathways but also significantly increases the electrode/electrolyte contact area, thereby enhancing the cycling stability and rate performance of silicon anodes.

Park *et al.*[65] successfully synthesized H-SiNTs *via* a template-assisted method involving the reduction and decomposition of a Si precursor within an alumina template, followed by an etching process. Fig. 7a shows that the nanotube structure dramatically increases the effective surface area of the electrode material, enabling simultaneous Li^+ insertion/extraction on both the inner and outer surfaces of the nanotubes. Fig. 7b

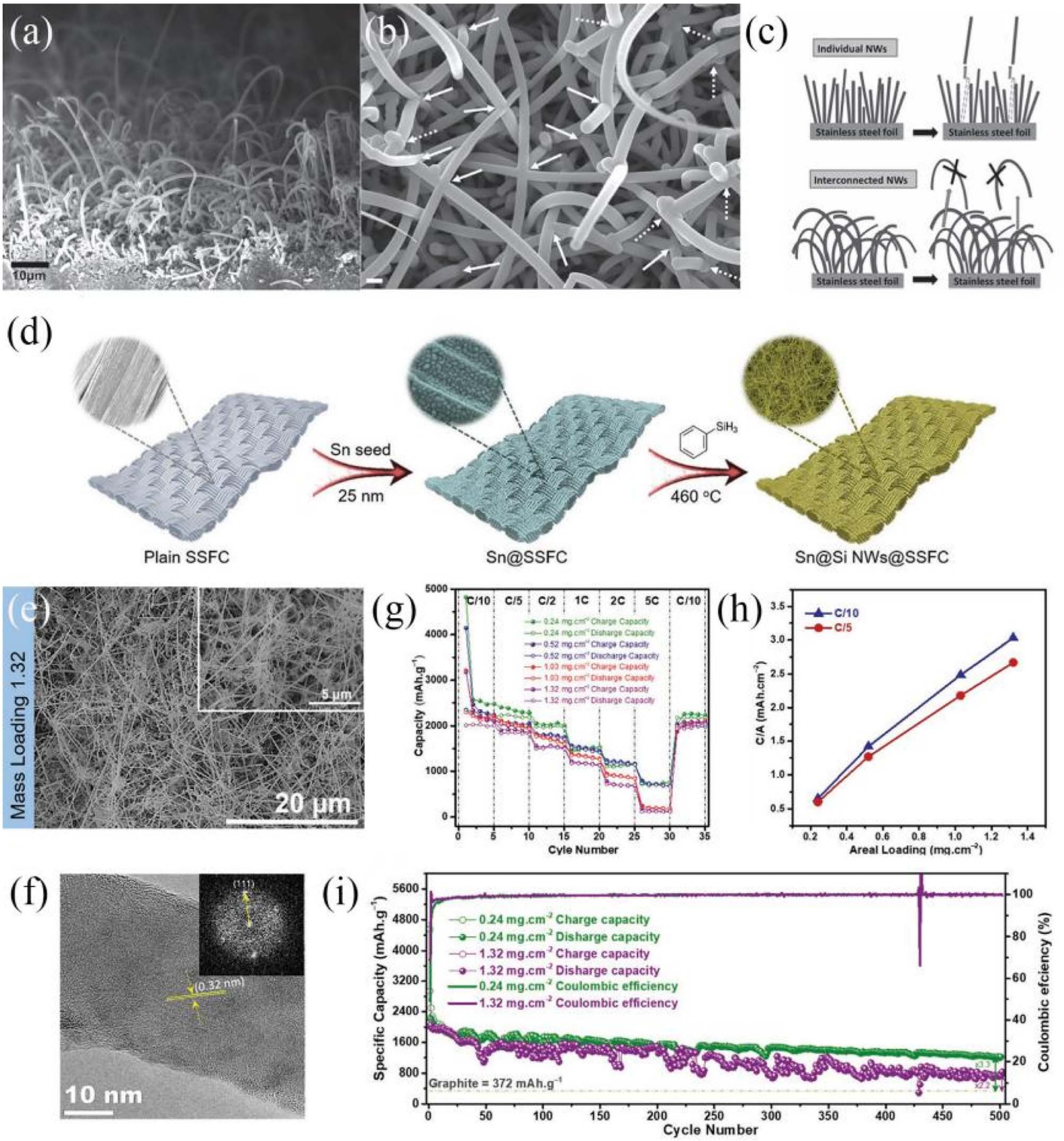

Fig. 6 (a) Cross-sectional SEM image of Si NWs; (b) top-view and magnified SEM images of Si NWs; (c) schematic illustration of the interconnection effect. (d) Schematic diagram of the synthesis of Sn-seeded Si NW@SSFC; (e) SEM image of the mass loading of 1.32 mg cm^{-2}; (f) TEM image of a single Sn-seeded Si NW; (g) rate performance of each loading at current densities of 0.1C, 0.2C, 0.5C, C, 2C, and 5C; (h) areal capacity (*C*/*A*) *versus* areal loading at 0.1C and 0.2C; (i) cycling performance curves of the samples with mass loadings of 0.24 and 1.32 mg cm^{-2}.

shows that the nanotube bundles are approximately 40 μm in length. The H-SiNTs anode exhibited excellent electrochemical performance, delivering a reversible capacity of 3247 mAh g^{-1} at 0.2C with ICE of 89%.

Wu *et al.*[57] further expanded the design concept of hollow Si nanotubes, and prepared a Si–SiO$_x$ nanotube (DWSiNT) anode with a unique double-walled structure *via* template method. The inner wall is composed of active Si, while the outer wall is made of SiO$_x$. Fig. 7c and d show the SEM morphologies of DWSiNTs in the initial state and after 2000 cycles, respectively. Even after 2000 cycles, only a thin SEI film is formed on the surface of DWSiNTs, and the structure of individual nanotubes can still be clearly observed. This double-walled structure design is crucial: the outer SiO$_x$ shell can effectively constrain

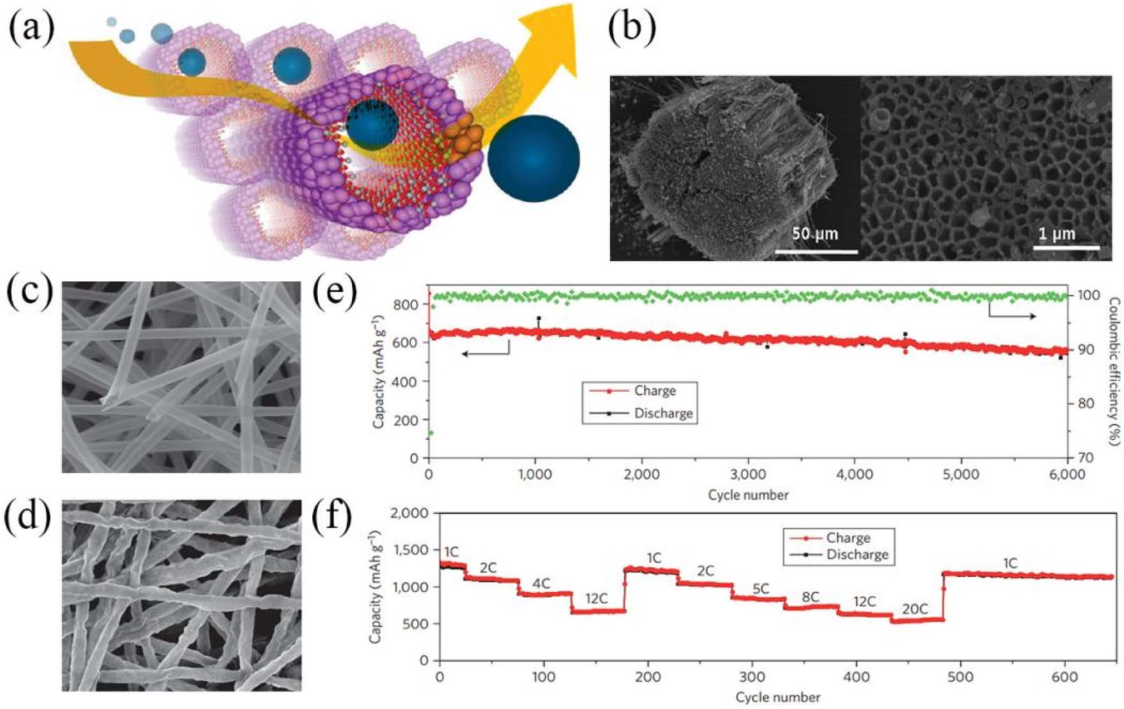

Fig. 7 (a) Schematic diagram of Li^+ pathways in Si nanotubes; (b) FE-SEM image of Si nanotubes. (c) SEM image of double-walled Si nanotubes (DWSiNT); (d) DWSiNT after 2000 cycles; (e) cycling performance curve at a rate of 10C and 12 °C; (f) rate performance plot of DWSiNT.

the volume expansion of the outer wall of Si nanotubes during cycling; meanwhile, the expanded inner Si layer is not directly exposed to the electrolyte, which inhibits the side reactions with the electrolyte. Therefore, the DWSiNTs anode exhibits an ultra-long cycle life and excellent rate performance. Fig. 7e shows that when cycled at an ultra-high rate of 10C, the DWSiNTs still retained 93% and 88% of their initial capacities after 4000 and 6000 cycles, respectively. The charge–discharge performance at different rates (Fig. 7f) is also outstanding. Even at an extremely high rate of 12C, the charge and discharge capacities (calculated based on the total mass of Si/DWSiNTs) can still reach 940 mAh g^{-1} and 600 mAh g^{-1}, respectively.

4.2.3 Nanospheres.

Compared with other structures, Si nanospheres have shown great potential in adapting to volume changes. Yao *et al.*[66] synthesized a novel interconnected Si hollow-sphere electrode (Fig. 8a) using chemical vapor deposition (CVD) technology. As shown in Fig. 8b, the structure consists of hollow spheres with an inner radius (R_{in}) of 175 nm and an outer radius (R_{out}) of 200 nm. The interconnected network effectively mitigates volume changes during cycling. This interconnected hollow structure not only buffers the stress caused by volume expansion/contraction but also facilitates rapid Li^+ diffusion, thereby enhancing the rate performance. The electrode maintained a capacity of 1420 mAh g^{-1} after 700 cycles with a coulombic efficiency (CE) of up to 99.5%, demonstrating excellent cycling stability.

Building on the nanosphere structure, Wang *et al.*[58] further designed mesoporous Si spheres (MPSS). Fig. 8c shows that the material was fabricated *via* a facile hydrolysis method combined with a surface-protected magnesiothermic reduction process. Fig. 8d reveals that MPSS exhibits highly monodisperse spherical morphology, which is beneficial for achieving uniform stress–strain distribution during charge–discharge cycles, thus significantly improving electrochemical stability. Notably, the specific surface area of MPSS (214.65 m^2 g^{-1}) is nearly an order of magnitude higher than that of SiO_2 nanospheres (SS, 20.07 m^2 g^{-1}) (Fig. 8e). Electrochemical tests showed that the capacity of MPSS-CNT decreased from 3000 mAh g^{-1} to 1000 mAh g^{-1} as the current density increased from 0.2C to 2C (Fig. 8f). After 500 cycles at 0.5C, the capacity remained above 1500 mAh g^{-1} with a capacity retention rate of 80% and a coulombic efficiency approaching 100% (Fig. 8g), indicating outstanding long-term cycling performance and interfacial stability.

4.2.4 Porous nano morphology.

Porous Si has emerged as an effective strategy to address the intrinsic drawbacks of silicon-based anode materials due to its unique pore structure. The pore space can effectively buffer the volume changes of Si while significantly shortening the diffusion path of Li^+. Kim *et al.*[67] reported a large-sized (>20 mm) three-dimensional (3D) porous Si particles prepared *via* a facile heat treatment method. As shown in Fig. 9a, the material exhibits an interconnected 3D porous network structure that effectively promotes Li^+ migration. This porous Si anode demonstrates excellent rate performance, with reversible discharge capacities of 2668 mAh g^{-1}, 2471 mAh g^{-1}, and 2158 mAh g^{-1} at 1C, 2C, and 3C rates, respectively. Moreover, it shows remarkable cycling stability,

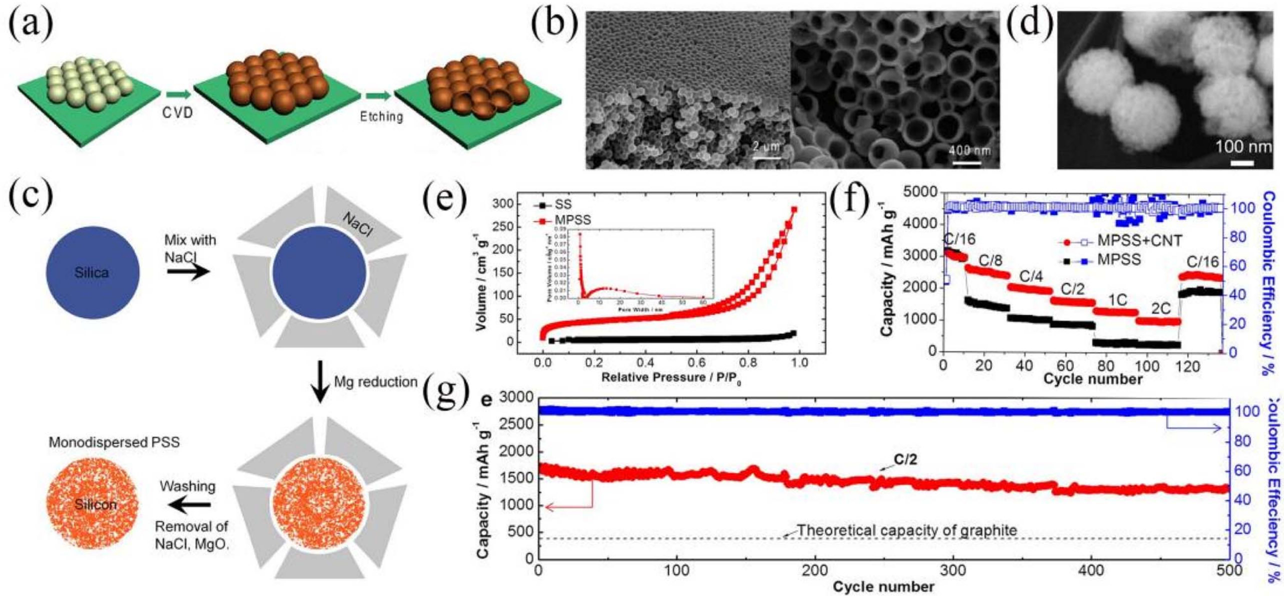

Fig. 8 (a) Schematic illustration of the synthesis of Si hollow nanospheres; (b) SEM images of hollow Si nanospheres in the initial state and after scratch treatment. (c) Schematic illustration of the synthesis of MPSS; (d) SEM image of MPSS; (e) BET specific surface area measurement of SS and MPSS from N_2 adsorption–desorption isotherms; (f) rate performance plots of MPSS electrodes with and without 2% CNTs; (g) cycling performance and CE curves of MPSS electrodes at 0.5C rate.

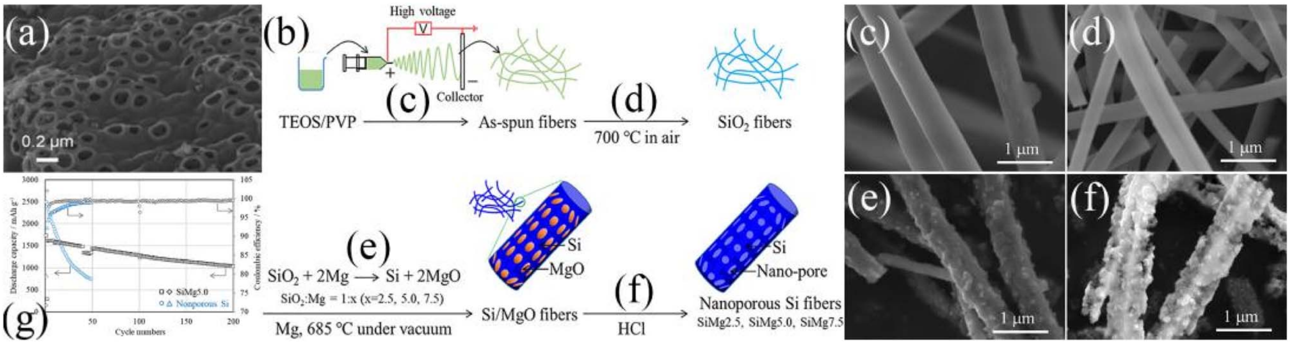

Fig. 9 (a) SEM image of porous Si particles. (b) Schematic illustration of the synthesis process for nanoporous Si fibers; SEM images of each step during the MPSS preparation: (c) as-spun fibers; (d) SiO_2 fibers after calcination in air; (e) SiMg5.0 before HCl etching and (f) SEM image of SiMg5.0. (g) Cycling performance curves of SiMg5.0 and nonporous Si anodes.

retaining 99% of its initial capacity after 100 cycles at 0.2C and 90% after cycling at 1C.

To tackle the interfacial compatibility challenges of sulfide-based solid electrolytes (SEs), Yamamoto *et al.*[59] designed and fabricated a composite anode SiMg5.0 based on a nanoporous Si fiber network structure, which combines electrospinning and magnesiothermic reduction techniques. Fig. 9b shows its preparation process, which mainly consists of four key steps: electrospinning (Fig. 9c), calcination (Fig. 9d), magnesiothermic reduction (Fig. 9e), and HCl etching (Fig. 9f). This unique structure endows the SiMg5.0 anode with excellent electrochemical performance (Fig. 9g). After 40 cycles, the reversible capacity is 1474 mAh g^{-1}, with a capacity retention rate of 85%. After 200 cycles, a capacity of 1038 mAh g^{-1} can still be maintained (capacity retention rate of 60%). This excellent performance is attributed to the fact that the total pore volume of the material during lithiation (formation of the $Li_{12}Si_7$ phase) can effectively compensate for the volume expansion of Si through pore shrinkage, suppressing the volume expansion and maintaining intimate contact at the Si–SE (or conductive additive) interface. Moreover, the Si fiber network structure formed after lithiation can compensate for the electron and ion conduction paths in partially delaminated regions that may occur during cycling, further enhancing the cycling stability of the electrode.

4.3 Composite structure design

The combination of silicon-based materials with functional materials is an effective approach to address the issues of Si anodes, such as volume expansion, interfacial instability, and low ionic/electronic conductivity. To date, researchers have developed various silicon-based composites, including Si–C,[68] $Si/Li_{21}Si_5$,[69] PL-Si/graphite,[70] $Si@SiO_2@LPO@C$,[71] Si@MgO@C.[72] Among them, carbon materials are regarded as ideal composite carriers due to their excellent electronic/ionic conductivity, mechanical properties, and compatibility with silicon, which can effectively suppress volume deformation during charge–discharge processes.[73,74]

There are diverse preparation techniques for silicon–carbon composites, with common methods including mechanical ball milling,[75] high-temperature pyrolysis,[76] CVD,[77] spray drying[78] and etching.[79] Structural design of materials can be achieved through process regulation, which further optimizes SEI stability, lithium ion/electron transport efficiency, suppression of electrolyte side reactions, and electrode structural integrity, thereby enhancing electrochemical performance.

Kim *et al.*[80] fabricated Si/CNF composites *via* electrospinning and constructed a conformal Li_6PS_5Cl (LPSCl) coating on their surface to enhance interfacial stability. Electrochemical tests revealed that the Si/CNF@LPSCl anode exhibited superior performance: a reversible capacity of 1172 mAh g^{-1} at 0.1C and a capacity retention of 84.3% after 50 cycles at 0.5C. At rates of 0.1C, 0.2C, 0.5C, and 1C, the reversible capacities were 1229 mAh g^{-1}, 881 mAh g^{-1}, 754 mAh g^{-1}, and 466 mAh g^{-1}, respectively. Kim *et al.*[60] prepared μSi/SWCNT/Li_6PS_5Cl composites through dispersion and calcination processes. During cycling, this composite anode effectively suppressed detrimental interfacial reactions between μSi particles and LPSCl and significantly mitigated volume expansion, thereby avoiding crack formation and contact failure. The anode demonstrated a high reversible capacity of 2974 mAh g^{-1} at 0.1C and maintained stability over 400 cycles. Compared to pure Si, its rate performance was remarkably enhanced, delivering 1271 mAh g^{-1} even at 1C. After 100, 200, 300, and 400 cycles, the capacity retentions were 75%, 66%, 58%, and 54%, respectively, with coulombic efficiencies consistently exceeding 99.5%. The combination of μSi and SWCNT played a critical role in maintaining interfacial stability with the LPSCl electrolyte, contributing to its excellent long-term cycling performance.

Han *et al.*[81] designed a self-integrated Si–N–MXene material. Fig. 10a shows the preparation flow chart of Si–N–MXene. The Si–N and N–MXene chemical bonds formed during the heat treatment process can effectively promote rapid lithium-ion/electron transport and maintain good mechanical stability. Meanwhile, the N–MXene framework provides an efficient Li^+ transport channel. It can be observed from Fig. 10b and c that micron Si particles are uniformly embedded on the MXene flakes. Based on this anode, a semi-solid-state battery Si–N–MXene/PEO@LATP/Li was assembled. Fig. 10d and e show that it has an initial specific capacity of 2305 mAh g^{-1} and an ICE of 82.02% at a current density of 0.2 A g^{-1}. After 10 cycles, the specific current increased to 0.4 A g^{-1}. The specific capacity was 1362 mAh g^{-1} at the 11th cycle and remained at 881 mAh g^{-1} after 90 cycles. For the $LiFePO_4$/PEO@LATP/Si–N–MXene full battery, Si–N–MXene still exhibits excellent electrochemical performance. The specific capacity at the first cycle was 1659.2 mAh g^{-1} at 0.32 A g^{-1}, and the capacity hardly decayed after 60 cycles (Fig. 10f and g). In addition, the mobility of adsorbed lithium ions was studied by density functional theory (DFT) calculations to further explore the electrochemical performance of Si–N–MXene in ASSBs. Fig. 10h shows two Li^+ diffusion pathways at the Si–N–MXene interface. The calculation results show that the migration energy barriers of Path-1 (Fig. 10i, 0.15 eV and 0.42 eV) are lower than those of Path-2 (Fig. 10j, 0.42 eV), indicating that Si–N atoms can improve the Li^+ mobility and thus promote charge transfer.

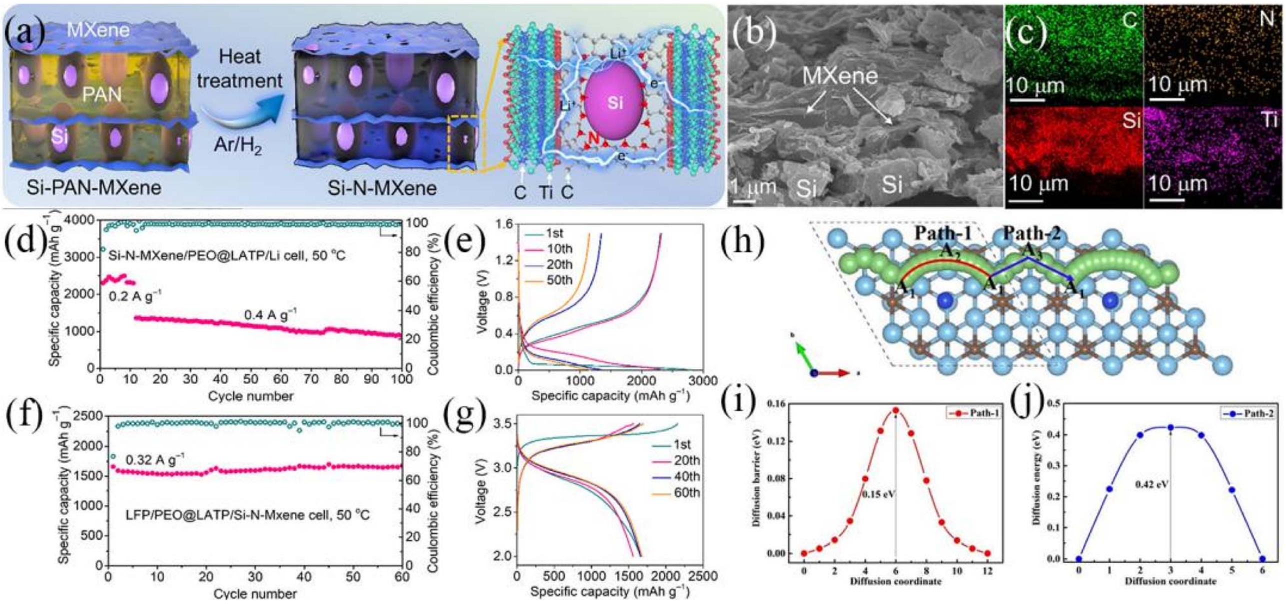

Fig. 10 (a) Schematic illustration of the preparation process for SiN–MXene; (b) SEM image of Si–N–MXene; (c) EDS image of Si–N–MXene; solid-state half-cell Si–N–MXene/PEO@LATP/Li: (d) charge–discharge voltage profiles at different cycles; (e) cycling performance plot. Full cell $LiFePO_4$/PEO@LATP/Si–N–MXene: (f) cycling performance plot; (g) charge–discharge voltage profiles at different cycles. (h) Li^+ diffusion pathways in Si–N–MXene. Diffusion energy barriers of Si–N–MXene: (i) Path-1; (j) Path-2.

Beyond carbon-based composites, the incorporation of non-carbon hosts offers a novel approach to enhance performance. In lithium–sulfur batteries, traditional carbon hosts struggle to suppress polysulfide shuttling due to their non-polar nature. In contrast, non-carbon hosts such as metals and metal compounds, leveraging the chemical adsorption capability of their polar surfaces and catalytic activity, can not only strengthen the confinement of active materials but also accelerate redox kinetics. Meanwhile, they circumvent the drawback of low tap density inherent to carbon materials.[82] This concept can be incorporated into the design of silicon-based composites: the introduction of polar non-carbon components (for example, MXenes, metal oxides) not only enhances mechanical confinement to alleviate the volume expansion of silicon but also stabilizes interfaces through chemical interactions. These components synergistically improve electrical conductivity and cycling stability, forming a complementary system to silicon–carbon composites.

4.4 New binder

Binder materials play a crucial role in maintaining the structural integrity of silicon-based anodes. Given the significant volume changes experienced by silicon during charge–discharge cycles, the development of high-performance binders with both excellent mechanical properties and chemical stability is of paramount importance. In SSBs, binders are additionally required to facilitate ionic transport.[83] To address these challenges, researchers have developed various specialized binder systems tailored for silicon-based anodes. Aqueous binders such as sodium carboxymethyl cellulose (CMC),[84,85] polyacrylic acid (PAA)[86] and polyimide (PI)[87] are widely recognized as particularly suitable for silicon-based anodes due to their unique properties.

Cave *et al.*[88] proposed an innovative strategy to dynamically regulate interfacial charge transfer kinetics by introducing permanent dipoles with labile characteristics at the electrode interface. This approach effectively mitigates capacity fade caused by continuous electrolyte reduction on silicon anodes. Fig. 11a shows two modification schemes for PAA using triethoxysilanes. The modifiers are classified into two categories based on the polarity and vibrational activity of their R-groups: 3-cyanopropyltriethoxysilane (CPTES), with a dipole moment along the carbon–nitrogen triple bond axis, is defined as a dipole modifier; vinyltriethoxysilane (VTES), with a nonpolar R-group, serves as a nonpolar modifier. Electrochemical tests (Fig. 11b) demonstrate that the CPTES-modified CPTES-PAA binder significantly enhances cycling stability, achieving a 17% higher capacity retention after 200 cycles compared to unmodified PAA.

Liu *et al.*[61] explored the feasibility of using gum arabic (GA) as a binder for Si particle anodes. Fig. 11c shows that GA is a polymeric polysaccharide, whose abundant hydroxyl groups can provide strong binding force, while the long-chain proteins endow the material with good mechanical properties. These combined effects effectively inhibit the volume expansion of Si particles during cycling. The Si anode using GA binder exhibits excellent ductility, which can effectively prevent the electrode from breaking due to volume change during charge–discharge processes. After 500 cycles at 1C and 2C rates, the specific capacities of the electrode remain at 2000 mAh g^{-1} and 1000 mAh g^{-1}, respectively. After 1000 cycles at 1C rate, the specific capacity still maintains above 1000 mAh g^{-1}, which fully demonstrates the good cycle stability of the electrode imparted by the GA binder.

This strategy of regulating stability through interfacial layer design has also been validated in other battery systems. In sodium-ion batteries, the Ag interfacial layer guides uniform Na deposition by its strong sodiophilicity and induces the formation of a NaF-rich inorganic SEI layer through strong interactions with PF_6^-, which effectively suppresses dendrite growth and side reactions, enabling the battery to cycle stably for over 1000 hours at 3 mA cm^{-2}.[89] In zinc batteries, the supramolecular polymer layer with donor–acceptor sites constructs

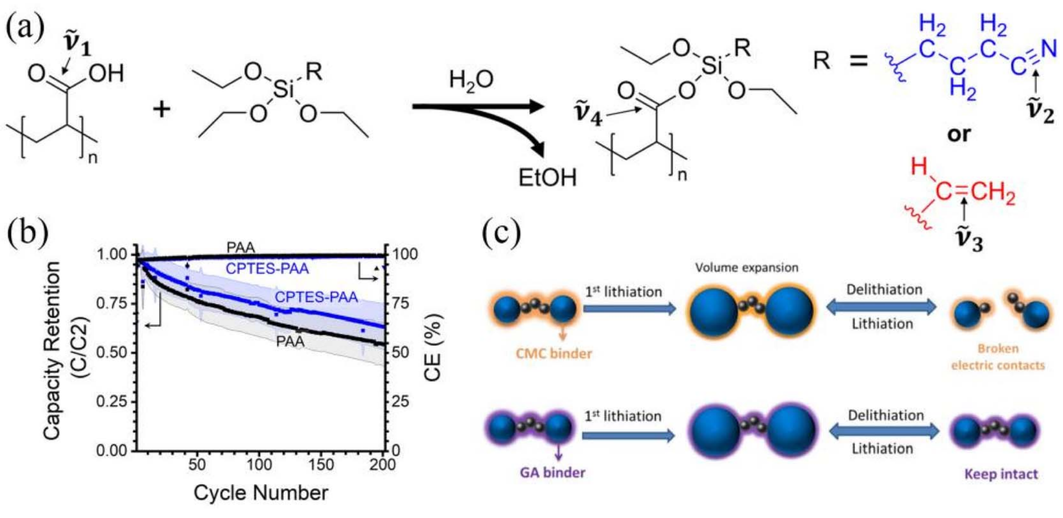

Fig. 11 (a) Two modification schemes for PPA. (b) Cycling performance curves of PPA and CPTES-PAA; (c) schematic diagrams of GA and CMC in response to volume changes.

a dynamic network *via* multivalent dipole interactions, which inhibits zinc dendrite growth under an ultrahigh mechanical modulus of 10.4 GPa while optimizing Zn^{2+} transport kinetics, resulting in a coulombic efficiency approaching 99.94% and stable cycling for 9000 cycles.[90] Similarly, such strategies can be adapted for silicon-based anodes. By designing functional binders (introducing dipole groups or regulating polar interactions) or composite interfacial layers, precise control over the composition and structure of the SEI can be achieved, thereby alleviating interface issues caused by the volume change of Si and further improving the cycling stability of the battery.

4.5 Current collector optimization

Silicon-based anodes undergo significant volume changes during charge and discharge cycles, which can easily lead to interfacial delamination between the anode and the current collector. This, in turn, causes the deactivation of active materials and capacity fade. Designing current collectors with special structures to effectively confine Si active materials within the current collector or strengthen their interfacial bonding is an effective strategy to suppress Si detachment and improve electrode stability.[91–93]

Jiang *et al.*[94] designed and fabricated a three-dimensional porous copper mesh current collector. This structure embeds Si particles within its internal voids, significantly enhancing the structural stability of the electrode and effectively suppressing the detachment of Si during cycling. Polat *et al.*[62] employed magnetron sputtering to deposit a copper layer on the surface of a Si anode, forming a CuSi thin layer. The CuSi layer can effectively anchor the Si material, preventing it from detaching from the current collector during volume expansion/contraction. Fig. 12 shows SEM images of the batteries after 3 and 30 galvanostatic cycles at a rate of C/12. After 3 cycles (Fig. 12a and b), the unmodified Si anode exhibited structural fractures, whereas the electrode modified with the CuSi layer maintained a regular structure. After 30 cycles (Fig. 12c and d), the structural fragmentation of the bare Si anode was severe. In contrast, only a few cracks appeared in the CuSi-modified electrode, demonstrating significantly improved structural integrity.

5 Solid-state electrolytes and compatibility with silicon-based anodes

After optimizing silicon-based anodes, it is necessary to match them with different types of SSEs to further improve the performance of SSBs. SSEs, as key component of SSBs, play a crucial role in ensuring battery performance and safety. Table 3 details several representative types of SSEs, including oxide SSEs, sulfide SSEs, polymer SSEs, and composite SSEs. These different types of SSEs each possess unique physicochemical properties and exhibit varying performances in terms of ionic conduction, mechanical properties and chemical stability, providing abundant options for the diversified design and performance optimization of silicon-based SSBs.

5.1 Oxide solid-state electrolytes

Oxide SSEs mainly include NASICON-type,[128,129] garnet-type,[130,131] perovskites,[132,133] anti-perovskites[134] and LiPON

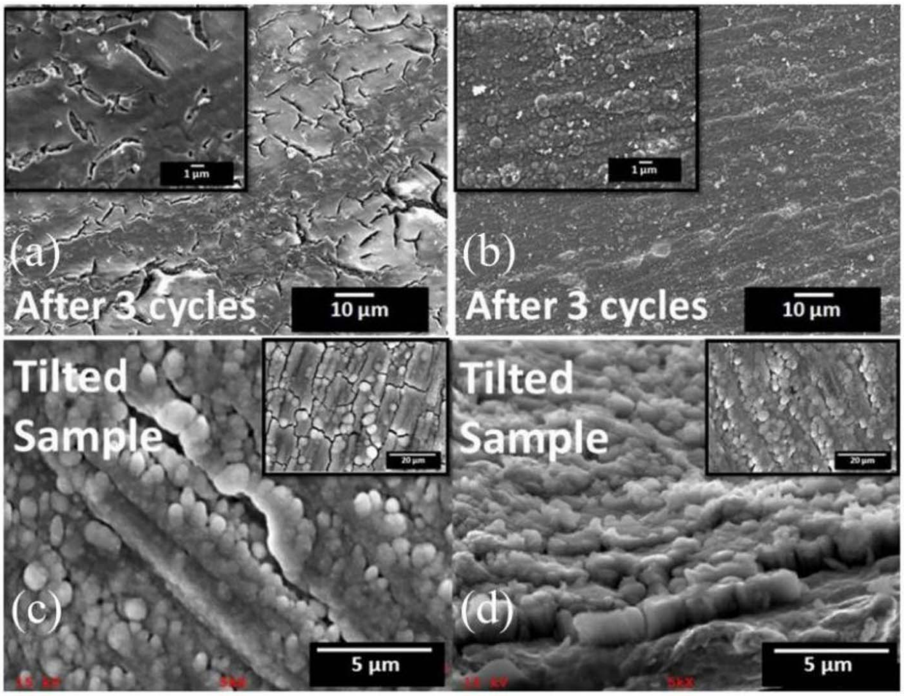

Fig. 12 SEM images of the electrodes after 3 cycles: (a) initial thin layer; (b) CuSi thin layer. SEM images of the electrodes after 30 cycles: (c) initial thin layer; (d) CuSi thin layer.

Table 3 Comparison of the characteristics of typical SSEs

Electrolyte type	Advantages	Limitations	Typical materials	Ionic conductivity (S cm^{-1})	Ref.
Oxide SSEs	High chemical and electrochemical stability, high mechanical strength, wide electrochemical window	Rigid structure	$Li_7La_3Zr_2O_{12}$	2.24×10^{-4}	95
			$(Li_{6.5}La_3Zr_{1.5}Ta_{0.5}O_{12})_{0.85}$–$(LiCl)_{0.15}$	1.22×10^{-3}	96
			$Li_7La_3Zr_{1.4}Ti_{0.6}O_{12}$	5.21×10^{-6}	97
			$Li_{6.03}La_3Zr_{1.533}Ta_{0.4}6O_{12}$	1.01×10^{-6}	97
		High processing temperature	$Li_{6.75}La_3Zr_{1.75}Nb_{0.25}O_{12}$	8×10^{-4}	98
			$Li_{7.1}La_3Zr_{1.95}Ca_{0.05}O_{12}$	5.2×10^{-4}	99
			$Li_{1.3}Al_{0.3}Ti_{1.7}(PO_4)_3$	1.21×10^{-3}	100
			$Li_6La_3Zr_{0.5}Hf_{0.5}Ta_{0.5}Nb_{0.5}O_{12}$	3.3×10^{-4}	101
		High interfacial resistance at the electrode–electrolyte interface	$Li_{6.4}Ga_{0.2}La_3Zr_{1.925}Y_{0.1}O_{12}$	1.04×10^{-3}	102
			b-$Li_{3.6}O_{3.4}N_{0.6}$	3.0×10^{-7}	103
			Fe–LiPON	1.08×10^{-5}	104
			Ti–LiPON	4.91×10^{-6}	105
Sulfide SSEs	Excellent electrical conductivity	Low oxidation stability	$Li_{10}SnP_2S_{12}$	4.0×10^{-3}	106
	High mechanical strength	Sensitivity to water	$Li_{9.5}Si_{1.74}P_{1.44}S_{11.7}Cl_{0.3}$	2.5×10^{-2}	107
	Wide electrochemical window	Low compatibility with cathode materials	$Li_{10}SiP_2S_{12}$	2.3×10^{-3}	108
			$Li_{11}SiP_2S_{12}$	2.3×10^{-3}	108
			$Li_{10}Ge_{0.95}Si_{0.05}P_2S_{12}$	8.6×10^{-3}	109
			$Li_{10}GeP_2S_{12}$	1.2×10^{-2}	110
			β-Li_3PS_4 (nanoporous)	1.6×10^{-4}	111
			$Li_{2.2}Zn_{0.1}Zr_{0.9}S_3$	1.2×10^{-4}	112
			$Li_6P_2S_4$	1.6×10^{-10}	113
			$Li_{6.5}In_{0.25}P_{0.75}S_5I$	1.06×10^{-3}	114
			Li_6PS_5Cl	1.1×10^{-2}	115
Polymer SSEs	High flexibility, good interfacial contact, low shear modulus	Low mechanical strength, narrow electrochemical window (<4 V), low ionic conductivity at room temperature	PECA	3.3×10^{-3}	116
			PEO/LiTFSl/$LiZr_2(PO_4)_3$	1.2×10^{-4}	117
			PEO/LiTFSl/Al_2O_3	4.4×10^{-5}	117
			pPEGMA	2.07×10^{-5}	118
			CSPE-B60	1.3×10^{-4}	119
			PEGMA/PEGDA	6.77×10^{-5}	120
			LDPPCCE	1.31×10^{-4}	121
			PV-PM-LA-SN	1.38×10^{-4}	122
Composite SSEs	Excellent comprehensive performance, high tunability	Complex preparation process, high cost	PEO/Ga-LLZO	7.2×10^{-5}	123
			PEO/LLZTO	1.12×10^{-5}	124
			PEO/LiTFSl/LLTO	8.8×10^{-5}	125
			PEO/LiTFSI	2.3×10^{-4}	126
			PI/PEO/LiTFSI	2.3×10^{-4}	9
			PEO-VAVS-LiTFSI	1.89×10^{-4}	9
			PSZ20	2.78×10^{-5}	127

group[135,136] electrolytes. These electrolytes have attracted extensive attention due to their relatively high room-temperature ionic conductivity (10^{-6}–10^{-3} S cm^{-1}), excellent chemical stability, and high mechanical strength.[137] Among these properties, the high mechanical strength is crucial for suppressing the significant volume expansion of silicon-based anode materials during charge–discharge processes. This greatly enhances the application potential of silicon-based materials in oxide solid-state battery systems, making them a current research hotspot.

Ping *et al.*[138] synthesized the cubic garnet-structured $Li_7La_3Zr_2O_{12}$ (LLZO) solid electrolyte *via* conventional solid-state sintering and paired it with a Si/CNT composite anode to construct SSBs. This battery exhibited exceptional electrochemical performance (a first-cycle discharge capacity of 2685 mAh g^{-1} and an ICE of 83.2% for the 1 μm-thick Si/CNT anode) and remarkable mechanical robustness. Mechanical modeling revealed that the high nanomechanical strength of LLZO effectively mitigated the volumetric expansion stress of the Si/CNT anode during lithiation. Simulations of crack propagation behavior during delithiation (Fig. 13a and b) showed that the maximum crack opening displacement in the anode was significantly reduced compared to LELIBs (Fig. 13c). Additionally, the state of charge (SOC) at which crack initiation occurred decreased from 36% to 20% (Fig. 13d). Furthermore, the garnet-based system conferred a lower crack driving force and higher fracture resistance to the Si anode, with reduced crack dissipation energy effectively limiting the shrinkage of the Si film during cycling degradation and minimizing active material loss.

Marumoto *et al.*[139] employed radio-frequency (RF) sputtering to fabricate a porous $SiO_{0.2}$ thick-film anode with high porosity, which was also integrated with LLZO. This design achieved excellent cycling stability (capacity retention of 82.9% and 75.9% after 100 cycles). The key advantage lies in the nano-scale interconnected pore structure, which acts as an effective buffer layer to alleviate internal and interfacial stresses generated during the lithiation/delithiation processes of $SiO_{0.2}$, thereby enhancing interfacial Li$^+$ transport. The study further demonstrated that increasing the thickness of the porous $SiO_{0.2}$ (for example, up to 5.0 μm) significantly boosted the areal discharge capacity, achieving an energy density approximately 17 times that of a typical 0.1 μm-thick non-porous $SiO_{0.2}$ electrode, thus providing a novel strategy for high-energy-density battery design.

5.2 Sulfide solid-state electrolytes

Sulfide SSEs can be classified into three categories based on their crystalline states: glassy, crystalline, and glass-ceramic ones.[140] Compared with other SSEs, they generally exhibit higher ionic conductivity (up to 10^{-2} S cm^{-1} at room temperature), moderate mechanical strength, and high-temperature stability, making them highly competitive in high-rate fast-charging batteries and high-energy-density energy storage systems.[141,142] These characteristics endow SSEs with broad application prospects in fields such as rapid energy replenishment for electric vehicles and power supply for electronic devices in extreme environments, and they are expected to become a key material system to break through the bottlenecks of existing energy storage technologies.

Poetke *et al.*[143] prepared the sulfide SSE Li_6PS_5Cl *via* mechanical ball milling. The battery constructed by matching it with a Si/C composite anode with a pre-designed void structure showed excellent cycle stability: at a current density of 0.2 mA

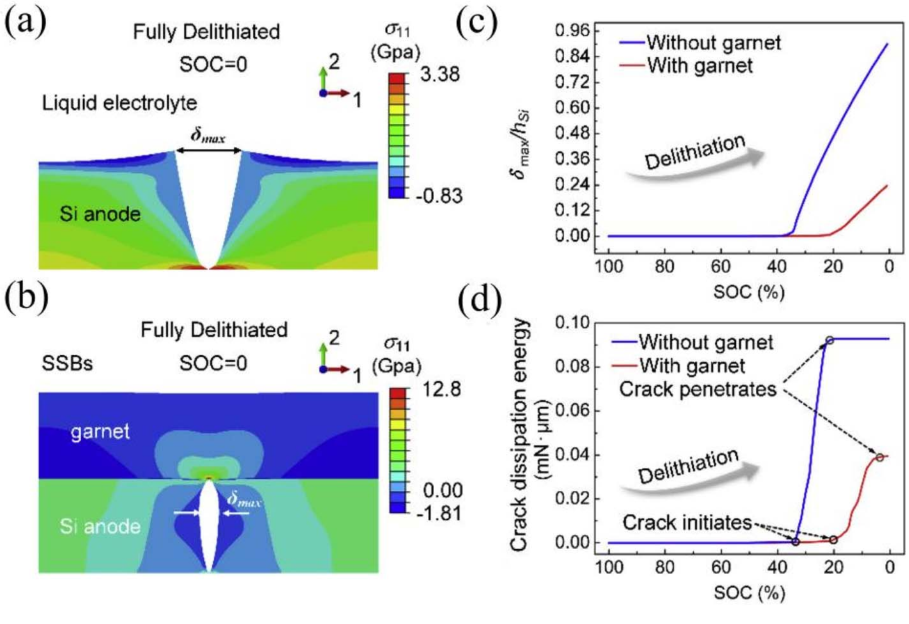

Fig. 13 Mechanical modeling of the morphology and normal in-plane stress distribution at the defective region of Si anodes in a fully delithiated state: (a) LELIBs; (b) SSBs. Parameter comparisons during delithiation without (blue) and with (red) LLZO: (c) maximum crack opening displacement (normalized by the Si anode thickness); (d) crack dissipation energy.

cm^{-2} (charging)/1.0 mA cm^{-2} (discharging), the capacity retention rate was as high as 87.7% after 50 cycles. Compared with LELIBs, this battery effectively suppressed interfacial side reactions, and the ICE was significantly improved (72.7% *vs.* 31.0%). It is worth noting that for practical applications, the areal capacity of silicon-based anodes needs to reach at least 4 mA cm^{-2}, which puts forward clear requirements for the design of battery energy density and cycle life.[29]

Cao *et al.*[144] designed and prepared a composite anode Si–SE–CB composed of nano-silicon, Li_6PS_5Cl (SE), and conductive carbon black (CB) through a ball milling process. Benefiting from the large contact area between nano-Si and SE as well as CB (Fig. 14a), the anode constructed a good electron/ion mixed conduction network on the entire electrode scale, thereby significantly improving its critical current density. In half-cell tests, the anode exhibited excellent rate performance: at current densities of 0.1, 0.2, 0.5, 1.0, and 2.0 mA cm^{-2}, the reversible capacities reached 2309, 2122, 1467, 802, and 440 mAh g^{-1}, respectively (Fig. 14b). The tolerable current density far exceeds the critical value of most reported lithium metals for sulfide electrolytes, highlighting the advantage of Si anodes over lithium metals in terms of compatibility with sulfide electrolytes. In addition, the half-cell still maintained a high reversible capacity of 1345 mAh g^{-1} after 200 cycles at 0.5 mA cm^{-2} (Fig. 14c). In the full-cell configuration (with Li_2SiO_x@S-NMC as the cathode), the system also showed excellent electrochemical performance, maintaining good stability after 1000 cycles at a C/3 rate (Fig. 14d).

Grandjean *et al.*[145] further investigated the compatibility characteristics between sulfide SSEs and silicon-based anodes. Two electrolytes with comparable ionic conductivities (LSnPS and LPSCl) were selected, and μSi was used as the active material for the tests. The results showed that the LPSCl half-cell exhibited a reversible capacity exceeding 2500 mAh g^{-1} in the first cycle, with an ICE of 90%. In contrast, the LSnPS half-cell delivered a capacity of less than 1000 mAh g^{-1} in the first cycle, with an ICE of only 40%, and its capacity degraded to 50% of the initial value by the 5th cycle. Moreover, the influence of Si size and morphology on the performance of the LPSCl electrolyte was studied. The results indicated that the half-cell with a SiNWs anode achieved an initial capacity of 2600 mAh g^{-1}, while the half-cell with a μSi anode showed a slightly higher initial capacity of 2700 mAh g^{-1}. However, at a current density of 0.1C, the SiNWs anode exhibited better cycling stability than the μSi anode. This is attributed to the superior dispersibility of SiNWs, which ensures good contact between electrode materials. In contrast, the μSi anode forms a thicker SEI film, leading to a reduction in exchange surface area and an increase in reactivity, thereby causing rapid capacity fading.

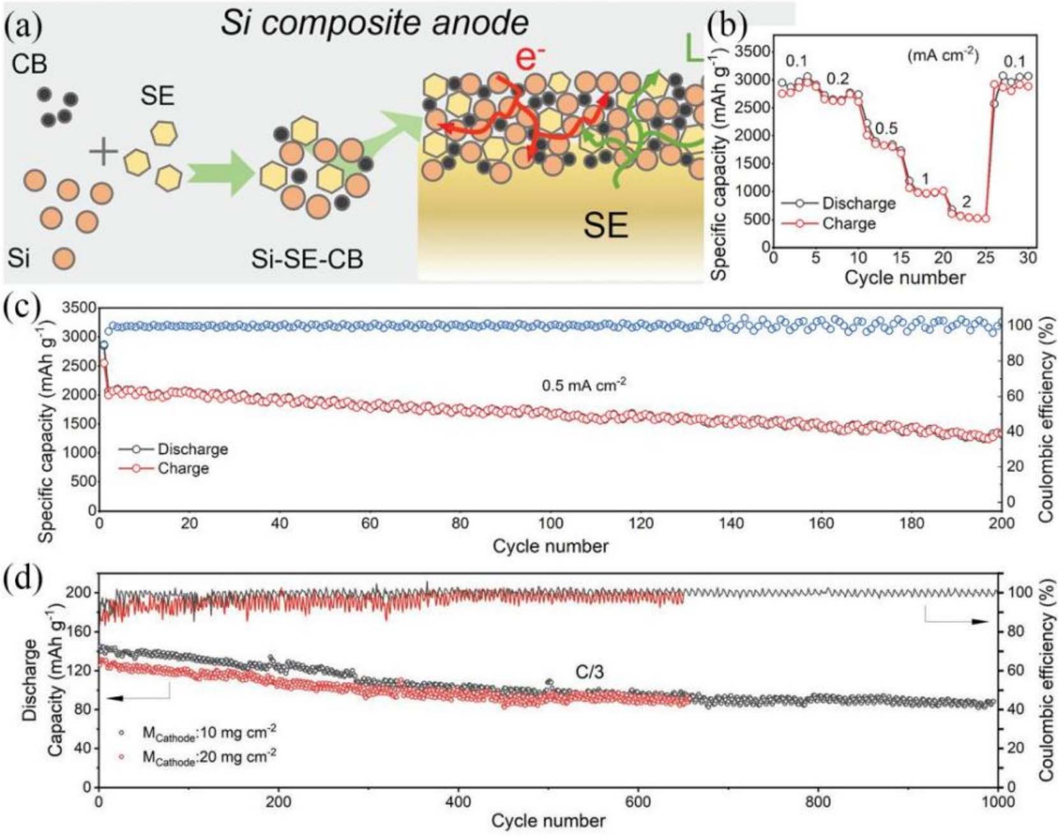

Fig. 14 (a) Schematic illustration of the preparation process of Si–SE–CB and the structure of the Si composite anode; (b) rate performance profiles at various current densities; (c) cycling performance curve at a current density of 0.5 mA cm^{-2}; (d) cycling performance curves of full cells with cathode mass loadings of 10 and 20 mg cm^{-2}.

5.3 Polymer solid-state electrolytes

The polymer SSEs consists mainly of a polymer matrix and lithium salts.[119] They are regarded as one of the most promising SSE systems due to their advantages such as simple preparation process, wide electrochemical window, light weight, low cost, low/non-volatility, and good processability.[146,147] In addition, the polymer SSE has high flexibility and low mobility, and the low mobility polymer electrolyte reacts only on the surface of Si to form a 2D SEI. 2D SEI can adapt to the volume change of Si particles during charging and discharging, maintain the stability of the SEI layer, and effectively improve the electrochemical performance of the Si-based anode.[148]

He *et al.*[42] developed a self-healing polymer SSE (SHDSE) for Si anodes using *in situ* polymerization technology. This electrolyte can form precise electrolyte–electrode interface contact at the molecular level (Fig. 15a), provide continuous and stable Li^+ transport channels, effectively inhibit the displacement of Si particles, and alleviate the volume expansion of electrodes. The Si|$LiCoO_2$ pouch cell constructed based on SHDSE exhibits excellent environmental tolerance and cycling stability: even under high temperature of 100 °C and continuous mechanical damage conditions (Fig. 15b), the cell can still maintain 86.2% of its discharge capacity after 30 000 mechanical bending cycles and 700 charge–discharge cycles, with an average coulombic efficiency exceeding 99.9%.

Wang *et al.*[148] constructed a 2D SEI film on the surface of the Si anode and designed a high-concentration polymer SSE (HCPE) by controlling the ring-opening polymerization of 1,3-dioxolane (DOL). The 2D SEI can adapt to the volume change of the Si particles and reduce the contact boundary area between the electrolyte and the Si particles. Furthermore, the low fluidity of HCPE inhibits the formation of 3D SEI films, further mitigates the occurrence of interfacial side reactions, and maintains a continuous Li^+/e^- transport pathway. Consequently, the battery assembled based on HCPE exhibits significantly improved electrochemical performance, delivering a capacity of up to 1765 mAh g^{-1} at a 2C rate and retaining a capacity of approximately 2000 mAh g^{-1} after 100 cycles at a 0.2C rate.

5.4 Composite solid-state electrolytes

Composite SSEs consist of two or more different electrolytes. Through composite strategies, they can effectively balance the performance limitations of single-component electrolytes, thereby enhancing their application potential in SSBs. Among them, polymer–inorganic composite SSEs are the most common: inorganic electrolytes (such as garnet-type and sulfide-type) usually provide high ionic conductivity and excellent mechanical strength, while flexible polymer electrolytes are beneficial for achieving good interfacial contact with electrodes. In recent years, due to their significant advantages, composite SSEs have become one of the important directions in the development of new electrolytes, and research has achieved certain outcomes.[149,150]

In terms of interface optimization and performance improvement, Huo *et al.*[151] constructed a flexible interface between the Si anode and composite solid polymer electrolytes (SPEs). The SPEs are composed of poly propylene carbonate (PPCs) and $Li_{6.4}La_3Zr_{1.4}Ta_{0.6}O_{12}$ (LLZTO), with an ionic conductivity of 4.2×10^{-4} S cm^{-1} at room temperature. The Si/SPE/Li battery assembled based on this exhibits excellent cycling stability: at a current density of 0.1C, the initial specific capacity is as high as 2675 mAh g^{-1}, and the capacity retention rate reaches 86.1% after 200 cycles. This performance is significantly better than that of the Si/LLZTO/Li battery (the capacity retention rate is only 49.1% after 200 cycles, and the coulombic efficiency is as low as 85.0%). The flexible interface between the Si anode and SPEs can effectively alleviate the interfacial stress caused by the volume change of the Si anode.

In terms of structural design and high-rate performance, Zhang *et al.*[152] designed a high-capacity SSB. Its composite SSEs PPG is composed of polyethylene oxide (PEO), $Li_{6.5}La_3Zr_{1.5}Ta_{0.5}O_{12}$ (garnet), and polyvinylidene fluoride (PVDF) fibers (Fig. 16a). Fig. 16b shows the internal structure of the battery

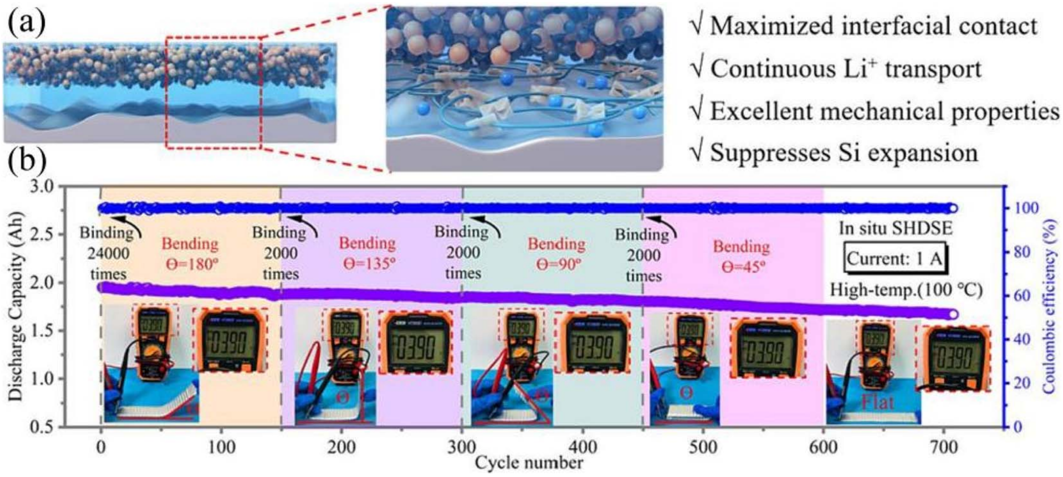

Fig. 15 (a) Schematic diagram of the Li|SHDSE|Si-SHDSE battery; (b) cycling performance curves of the SHDSE-based Si|$LiCoO_2$ pouch cell under harsh operating conditions of high temperature and continuous damage.

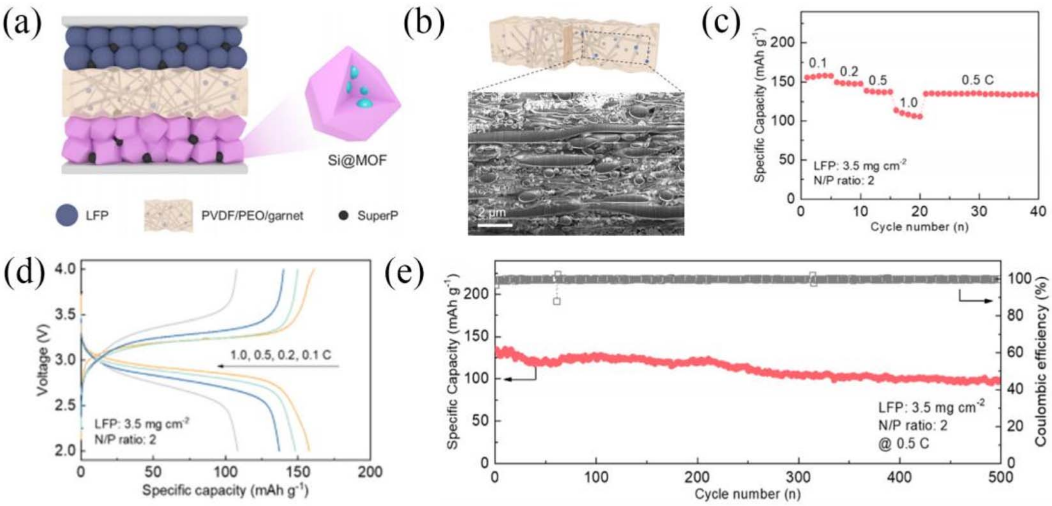

Fig. 16 (a) Schematic illustration of the LFP|PPG|Si@MOF SSB configuration; (b) internal structure of the PPG layer after focused ion beam (FIB) cutting. Electrochemical performance of the Si@MOF|PPG|LFP full cell at various current densities: (c) discharge capacity, (d) voltage profiles, (e) cycling performance of the Si@MOF|PPG|LFP cell at 0.5C.

revealed by vertical cutting with a focused ion beam (FIB). The circular regions formed by PVDF fibers enhance the mechanical properties of PPG, while the dispersed nano-garnet particles significantly improve the ionic conductivity and facilitate the rapid transport of Li^+ ions. The full cell composed of PPG and silicon-based anode exhibits excellent electrochemical performance. Fig. 16c and d show that at a high rate of 1.0C, the Si@MOF full cell can still provide a capacity of 108 mAh g^{-1}, indicating good rate capability, and achieves an excellent capacity retention rate of 73.1% after 500 cycles (Fig. 16e). This demonstrates the effectiveness of the battery design strategy based on PPG electrolyte and silicon-based anode in achieving long-term cycling stability.

5.5 Analysis and comparison of solid-state electrolytes

Based on the above, the compatibility of different SSEs with silicon-based anodes is evaluated from three aspects: mechanical strength (to suppress Si volume expansion), interfacial stability (to reduce contact failure), and ionic conductivity (to compensate for the low intrinsic conductivity of Si). The specific analysis is as follows:

5.5.1 Oxide SSEs. Oxide SSEs exhibit moderate ionic conductivity and ultrahigh mechanical strength. For instance, perovskite-type $Li_xLa_{0.5}TiO_3$ has a Young's modulus of 72–148 GPa (increasing significantly with Li_2O content), which can effectively constrain the volume expansion of Si particles and reduce electrode cracking and pulverization.[153] Oxide SSEs are suitable for scenarios requiring high long-term cycling stability (for example, grid energy storage). However, they are extremely brittle and have poor interface contact with Si. Moreover, materials like $Li_7La_3Zr_2O_{12}$ (LLZO) tend to form impurities such as Li_2CO_3 when exposed to air, leading to a sharp increase in interfacial resistance.[154] The compatibility with silicon-based anodes can be improved by interfacial modification (for example, Li–Na eutectic alloy), which reduces the impedance from 572 Ω cm^2 to 19 Ω cm^2 (at 60 °C).[155]

5.5.2 Sulfide SSEs. Sulfide SSEs offer the highest ionic conductivity (LGPS, 10^{-2} S cm^{-1}) and moderate mechanical toughness (Young's modulus of 18–25 GPa for Li_2S–P_2S_5 glass electrolytes), enabling them to adapt to the volume change of Si through elastic deformation. This property, combined with low interfacial resistance, results in high compatibility with silicon-based anodes.[156] For example, the combination of μSi/SWCNT with LPSCl delivers a capacity of 2974 mAh g^{-1} at 0.1C and maintains stability over 400 cycles, making it suitable for high-power scenarios (for example, electric vehicle fast charging).[60] Nevertheless, these electrolytes are sensitive to moisture and undergo slight side reactions with Si, requiring strict humidity control during preparation, which limits their practicality.

5.5.3 Polymer SSEs. The ionic conductivity of polymer SSEs is temperature-dependent (reaching 10^{-4} S cm^{-1} at 60 °C), with poor ionic conductivity at low temperatures. They also exhibit low mechanical strength (Young's modulus of 1.5 GPa for EP/GF-CPE), making it difficult to suppress lithium dendrite growth (which requires an elastic modulus >9 GPa).[157,158] Nevertheless, electrolytes such as PEO, polyacrylonitrile (PAN), and PPC possess relatively low interfacial resistance and flexibility, ensuring good interfacial contact with silicon and mitigating the impact of volume changes caused by Si.[123] Self-healing polymers (for example, SHDSE) further enhance adaptability to silicon deformation, maintaining stable contact even under continuous mechanical damage, making them suitable for flexible, low-rate electronic devices.[42]

5.5.4 Composite SSEs. Composite SSEs exhibit moderate ionic conductivity and mechanical strength (Young's modulus of 15 GPa for CSSE), and can be compatible with various Si structures (nanowires, porous structures, nanospheres).[158] The resistance can be reduced by designing composite electrolytes, and inorganic fillers (for example, LLZO) can be added to improve ionic conductivity and chemical stability.[149] However, the complex preparation process and high cost of composite SSEs limit their large-scale application, although they are suitable for scenarios demanding both energy density and power density.

6 Summary and outlook

Silicon-based materials are regarded as ideal candidates for fabricating high-energy-density and high-safety SSBs, owing to their superior properties such as a high theoretical capacity (4200 mAh g^{-1}), a low lithium insertion potential (0.4 V *vs.* Li^+/Li), and abundant natural reserves (accounting for 27.7% of the Earth's crust). In this work, the challenges faced by silicon-based anodes and the unique opportunities existing in the SSE system are reviewed. Furthermore, aiming at the issues of silicon-based materials including volume change, SEI problems, kinetic sluggishness, and interfacial impedance, the proposed multi-level optimization strategies are as follows:

6.1 Intrinsic material modification (alloying and nano-structuring)

Alloying, through the formation of alloys with metallic elements, can effectively enhance the electrical conductivity of silicon-based materials and improve their mechanical stability. However, alloying elements may reduce the material capacity, and their long-term cycling stability still needs further verification. Nano-structuring, *via* size regulation and structural design, can effectively alleviate the volume effect of silicon-based materials, shorten ion diffusion paths, and increase reactive active sites. Nevertheless, the large specific surface area of nanomaterials will aggravate interfacial side reactions, and their high cost is unfavorable for commercialization.

6.2 Composite structure design

Compositing Si with carbon materials or other functional materials can suppress the volume change of Si, construct conductive networks to enhance electrical conductivity, and improve cycling life. However, the Si content in composite materials is limited, which affects the overall capacity and volumetric energy density, and the interface engineering is complex.

6.3 Electrode structure optimization (binders and current collectors)

New binders can effectively maintain the structural integrity of electrodes and improve ionic stability. However, some binders have insufficient ionic conductivity, and adding an appropriate amount of binders can avoid the reduction of energy density. Ideal current collectors can effectively inhibit lithium dendrite growth and improve electrical contact. However, complex current collector structures will increase costs and process difficulties.

6.4 Electrolyte matching optimization

Oxide SSEs exhibit high mechanical strength and chemical stability but suffer from high interfacial resistance. Sulfide SSEs possess high ionic conductivity and moderate toughness yet are sensitive to moisture. Polymer SSEs feature excellent flexibility and electrode contact, while their ionic conductivity and mechanical strength are relatively low. In contrast, composite SSEs can be tailored through rational design to suit diverse application scenarios.

In summary, sulfide SSEs are considered the most suitable choice for matching with silicon-based materials due to their high ionic conductivity, moderate mechanical strength, and excellent interfacial stability.

Beyond the aforementioned strategies, future research should focus on the following directions. Design multifunctional coatings with dynamic adaptive capabilities (such as metals, metal oxides, or carbon materials) to inhibit side reactions between Si and electrolytes, promote Li^+ conduction, and adapt to the continuous volume changes of Si during cycling. Develop new types of SSEs with high ionic conductivity, good interfacial compatibility, and high mechanical strength, while improving their air stability to reduce manufacturing costs. In addition, pre-lithiation technologies and interfacial engineering methods used for silicon-based anodes in LIBs can be adopted to address the low ICE and interfacial side reactions in SSBs, thereby enhancing the cycle life of SSBs. Despite the fact that the application of silicon-based materials in SSBs still confronts challenges such as high material preparation costs, difficulties in regulating interfacial impedance, and immature large-scale production processes, the utilization of silicon-based materials in SSBs remains a crucial direction for future development. It is anticipated that this work will provide new insights into the future research and application of silicon-based anodes.

Conflicts of interest

The authors declare that they have no conflict of interest.

Data availability

No primary research results, software, or code have been included, and no new data were generated or analysed as part of this review.

Acknowledgements

Project supported by the 2022 Central Guided Local Science and Technology Development Funding Project (ZY20220102) and 2022 China Nonferrous Group Science and Technology Program (2022KJZX04).

References

1 H. Li, Practical Evaluation of Li-Ion Batteries, *Joule*, 2019, **3**(4), 911–914.

2 H. Wu and Y. Cui, Designing nanostructured Si anodes for high energy lithium ion batteries, *Nano Today*, 2012, **7**(5), 414–429.

3 S. Ponnada, M. S. Kiai, R. Krishnapriya, R. Singhal and R. K. Sharma, Lithium-Free Batteries: Needs and Challenges, *Energy Fuels*, 2022, **36**(12), 6013–6026.

4 W. Xu, J. Wang, F. Ding, X. Chen, E. Nasybulin, Y. Zhang and J. Zhang, Lithium metal anodes for rechargeable batteries, *Energy Environ. Sci.*, 2014, **7**(2), 513–537.

5 T. Krauskopf, R. Dippel, H. Hartmann, K. Peppler, B. Mogwitz, F. H. Richter, W. G. Zeier and J. Janek, Lithium-Metal Growth Kinetics on LLZO Garnet-Type Solid Electrolytes, *Joule*, 2019, **3**(8), 2030–2049.

6 X. Gao, Y. Zhou, D. Han, J. Zhou, D. Zhou, W. Tang and J. B. Goodenough, Thermodynamic Understanding of Li-Dendrite Formation, *Joule*, 2020, **4**(9), 1864–1879.

7 X. Cheng, C. Zhao, Y. Yao, H. Liu and Q. Zhang, Recent Advances in Energy Chemistry between Solid-State Electrolyte and Safe Lithium-Metal Anodes, *Chem*, 2019, **5**(1), 74–96.

8 B. Chen, J. Zhang, T. Zhang, R. Wang, J. Zheng, Y. Zhai and X. Liu, Constructing a Superlithiophilic 3D Burr-Microsphere Interface on Garnet for High-Rate and Ultra-Stable Solid-State Li Batteries, *Adv. Sci.*, 2023, **10**(11), e2207056.

9 L. Xu, J. Li, H. Shuai, Z. Luo, B. Wang, S. Fang, G. Zou, H. Hou, H. Peng and X. Ji, Recent advances of composite electrolytes for solid-state Li batteries, *J. Energy Chem.*, 2022, **67**, 524–548.

10 M. Kim, H. Ahn, J. Choi and W. B. Kim, A Rational Design of Silicon-Based Anode for All-Solid-State Lithium-Ion Batteries: A Review, *Energy Technol.*, 2023, **11**(6), 2201321.

11 C. Chen, A. Liang, C. Huang, T. Hsu and Y. Li, The pitch-based silicon-carbon composites fabricated by electrospraying technique as the anode material of lithium ion battery, *J. Alloys Compd.*, 2020, **844**, 156025.

12 M. Sohn, D. S. Kim, H. I. Park, J. H. Kim and H. Kim, Porous Silicon–Carbon Composite Materials Engineered by Simultaneous Alkaline Etching for High-Capacity Lithium Storage Anodes, *Electrochim. Acta*, 2016, **196**, 197–205.

13 Y. Deng, X. Feng, Z. Qian, J. Ma, Y. Ouyang, W. Li and C. Han, Silicon anode modification strategies in solid-state lithium-ion batteries, *Mater. Horiz.*, 2025, **12**(15), 5513–5538.

14 X. Zhao, Y. Rong, Y. Duan, Y. Wu, D. He, X. Qi and J. Wang, Development of Si-Based Anodes for All-Solid-State Li-Ion Batteries, *Coatings*, 2024, **14**(5), 608.

15 A. Song, W. Zhang, H. Guo, L. Dong, T. Jin, C. Shen and K. Xie, A Review on the Features and Progress of Silicon Anodes-Based Solid-State Batteries, *Adv. Energy Mater.*, 2023, **13**(39), 2301464.

16 J. Janek and W. G. Zeier, Challenges in speeding up solid-state battery development, *Nat. Energy*, 2023, **8**(3), 230–240.

17 J. Entwistle, A. Rennie and S. Patwardhan, A review of magnesiothermic reduction of silica to porous silicon for lithium-ion battery applications and beyond, *J. Mater. Chem. A*, 2018, **6**(38), 18344–18356.

18 X. H. Liu, L. Zhong, S. Huang, S. X. Mao, T. Zhu and J. Y. Huang, Size-Dependent Fracture of Silicon Nanoparticles During Lithiation, *ACS Nano*, 2012, **6**(2), 1522–1531.

19 P. Verma, P. Maire and P. Novák, A review of the features and analyses of the solid electrolyte interphase in Li-ion batteries, *Electrochim. Acta*, 2010, **55**(22), 6332–6341.

20 C. K. Chan, R. Ruffo, S. S. Hong and Y. Cui, Surface chemistry and morphology of the solid electrolyte interphase on silicon nanowire lithium-ion battery anodes, *J. Power Sources*, 2009, **189**(2), 1132–1140.

21 X. Wu, Z. Wang, L. Chen and X. Huang, Ag-enhanced SEI formation on Si particles for lithium batteries, *Electrochem. Commun.*, 2003, **5**(11), 935–939.

22 H. T. Nguyen, F. Yao, M. R. Zamfir, C. Biswas, K. P. So, Y. H. Lee, S. M. Kim, S. N. Cha, J. M. Kim and D. Pribat, High-performance lithium battery anodes using silicon nanowires, *Nat. Nanotechnol.*, 2008, **3**(1), 31–35.

23 L. Xu, S. Tang, Y. Cheng, K. Wang, J. Liang, C. Liu, Y. Cao, F. Wei and L. Mai, Interfaces in Solid-State Lithium Batteries, *Joule*, 2018, **2**(10), 1991–2015.

24 M. A. Rahman, G. Song, A. I. Bhatt, Y. C. Wong and C. Wen, Nanostructured Silicon Anodes for High-Performance Lithium-Ion Batteries, *Adv. Funct. Mater.*, 2015, **26**(5), 647–678.

25 Y. Ouyang, X. Zhu, F. Li, F. Lai, Y. Wu, Y.-E. Miao and T. Liu, Silicon @ nitrogen-doped porous carbon fiber composite anodes synthesized by an in-situ reaction collection strategy for high-performance lithium-ion batteries, *Appl. Surf. Sci.*, 2019, **475**, 211–218.

26 D. Shen, C. Huang, L. Gan, J. Liu, Z. Gong and M. Long, Rational Design of Si@SiO_2/C Composites Using Sustainable Cellulose as a Carbon Resource for Anodes in Lithium-Ion Batteries, *ACS Appl. Mater. Interfaces*, 2018, **10**(9), 7946–7954.

27 N. Ding, J. Xu, Y. X. Yao, G. Wegner, X. Fang, C. H. Chen and I. Lieberwirth, Determination of the diffusion coefficient of lithium ions in nano-Si, *Solid State Ionics*, 2009, **180**(2–3), 222–225.

28 K. Wen, M. Xia, P. Deng, W. Lv and W. He, A sandwich-structured double-battery device for direct evaluation of lithium diffusion coefficients and phase transition in electrodes of lithium ion batteries, *Chem. Eng. Sci.*, 2019, **200**, 80–86.

29 F. Boorboor Ajdari, P. Asghari, A. Molaei Aghdam, F. Abbasi, R. P. Rao, A. Abbasi, F. Ghasemi, S. Ramakrishna and N. Mikaeili Chahartagh, Silicon Solid State Battery: The Solid-State Compatibility, Particle Size, and Carbon Compositing for High Energy Density, *Adv. Funct. Mater.*, 2024, **34**(30), 2314822.

30 N. Kim, S. Chae, J. Ma, M. Ko and J. Cho, Fast-charging high-energy lithium-ion batteries via implantation of amorphous silicon nanolayer in edge-plane activated graphite anodes, *Nat. Commun.*, 2017, **8**(1), 812.

31 H. Kim, K. E. Kweon, C. Chou, J. G. Ekerdt and G. S. Hwang, On the Nature and Behavior of Li Atoms in Si: A First

Principles Study, *J. Phys. Chem. C*, 2010, **114**(41), 17942–17946.

32 Y. Jiang, G. Offer, J. Jiang, M. Marinescu and H. Wang, Voltage Hysteresis Model for Silicon Electrodes for Lithium Ion Batteries, Including Multi-Step Phase Transformations, Crystallization and Amorphization, *J. Electrochem. Soc.*, 2020, **167**(13), 130533.

33 D. H. Kim, S. Hwang, J. J. Cho, S. Yu, S. Kim, J. Jeon, K. H. Ahn, C. Lee, H. K. Song and H. Lee, Toward Fast Operation of Lithium Batteries: Ion Activity as the Factor To Determine the Concentration Polarization, *ACS Energy Lett.*, 2019, **4**(6), 1265–1270.

34 G. Hou, B. Cheng, Y. Cao, M. Yao, B. Li, C. Zhang, Q. Weng, X. Wang, Y. Bando, D. Golberg and F. Yuan, Scalable production of 3D plum-pudding-like Si/C spheres: Towards practical application in Li-ion batteries, *Nano Energy*, 2016, **24**, 111–120.

35 H. J. Kwon, J. Y. Hwang, H. J. Shin, M. G. Jeong, K. Y. Chung, Y. K. Sun and H. G. Jung, Nano/Microstructured Silicon-Carbon Hybrid Composite Particles Fabricated with Corn Starch Biowaste as Anode Materials for Li-Ion Batteries, *Nano Lett.*, 2020, **20**(1), 625–635.

36 Z. Liu, Q. Yu, Y. Zhao, b. R. He, M. Xu, S. Feng, S. Li, L. Zhou and L. Mai, Silicon oxides: a promising family of anode materials for lithium-ion batteries, *Chem. Soc. Rev.*, 2019, **48**(1), 285–309.

37 G. Zhu, F. Zhang, X. Li, W. Luo, L. Li, H. Zhang, L. Wang, Y. Wang, W. Jiang, H. K. Liu, S. X. Dou and J. Yang, Engineering the Distribution of Carbon in Silicon Oxide Nanospheres at the Atomic Level for Highly Stable Anodes, *Angew. Chem., Int. Ed.*, 2019, **58**(20), 6669–6673.

38 A. Manthiram, X. Yu and S. Wang, Lithium battery chemistries enabled by solid-state electrolytes, *Nat. Rev. Mater.*, 2017, **2**(4), 16103.

39 Z. Zhang, X. Zhang, Y. Liu, C. Lan, X. Han, S. Pei, L. Luo, P. Su, Z. Zhang, J. Liu, Z. Gong, C. Li, G. Lin, C. Li, W. Huang, M.-S. Wang and S. Chen, Silicon-based all-solid-state batteries operating free from external pressure, *Nat. Commun.*, 2025, **16**(1), 1013.

40 T. Bok, S. J. Cho, S. Choi, K. H. Choi, H. Park, S. Lee and S. Park, An effective coupling of nanostructured Si and gel polymer electrolytes for high-performance lithium-ion battery anodes, *RSC Adv.*, 2016, **6**(9), 6960–6966.

41 Q. Li, X. Wang, S. Zhu, Q. Zhong, S. Liu and Q. Zhou, Fast Li-ion conduction enabled by graphite fluoride flakes in solid polymer electrolyte, *Rare Met.*, 2023, **42**(10), 3337–3344.

42 S. He, S. Huang, X. Liu, X. Zeng, H. Chen, L. Zhao, H. Noor and X. Hou, Interfacial self-healing polymer electrolytes for Long-Cycle silicon anodes in High-Performance solid-state lithium batteries, *J. Colloid Interface Sci.*, 2024, **665**, 299–312.

43 G. Ferraresi, M. El Kazzi, L. Czornomaz, C. L. Tsai, S. Uhlenbruck and C. Villevieille, Electrochemical Performance of All-Solid-State Li-Ion Batteries Based on Garnet Electrolyte Using Silicon as a Model Electrode, *ACS Energy Lett.*, 2018, **3**(4), 1006–1012.

44 D. H. S. Tan, Y. Chen, H. Yang, W. Bao, B. Sreenarayanan, J. M. Doux, W. Li, B. Lu, S. Y. Ham, B. Sayahpour, J. Scharf, E. A. Wu, G. Deysher, H. E. Han, H. J. Hah, H. Jeong, J. B. Lee, Z. Chen and Y. S. Meng, Carbon-free high-loading silicon anodes enabled by sulfide solid electrolytes, *Science*, 2021, **373**(6562), 1494–1499.

45 D. Liu, Z. Liu, X. Li, W. Xie, Q. Wang, Q. Liu, Y. Fu and D. He, Group IVA Element (Si, Ge, Sn)-Based Alloying/Dealloying Anodes as Negative Electrodes for Full-Cell Lithium-Ion Batteries, *Small*, 2017, **13**(45), 1613–6810.

46 W. Zhang, A review of the electrochemical performance of alloy anodes for lithium-ion batteries, *J. Power Sources*, 2011, **196**(1), 13–24.

47 P. Zheng, J. Sun, H. Liu, R. Wang, C. Liu, Y. Zhao, J. Li, Y. Zheng and X. Rui, Microstructure Engineered Silicon Alloy Anodes for Lithium-Ion Batteries: Advances and Challenges, *Batteries Supercaps*, 2022, **6**(1), e202200481.

48 J. Zhou, J. Qin and H. Zhan, Copper Current Collector: The Cornerstones of Practical Lithium Metal and Anode-Free Batteries, *Chemphyschem*, 2024, **25**(8), e202400007.

49 Z. Cai, Z. Xu, N. Zhang, T. Peng, Y. Tan, H. Zhong, X. Liu and Y. Mai, Understanding Electrochemical Reaction Mechanisms of All-Electrochem-Active Mg_2Si Electrode in All-Solid-State Batteries, *Inorg. Chem.*, 2024, **63**(47), 22542–22548.

50 H. L. Xiao, L. Zhong, S. Huang, S. X. Mao, T. Zhu and J. Y. Huang, Size-Dependent Fracture of Silicon Nanoparticles During Lithiation, *ACS Nano*, 2012, **6**(2), 1522–1531.

51 X. Shen, Z. Tian, R. Fan, L. Shao, D. Zhang, G. Cao, L. Kou and Y. Bai, Research progress on silicon/carbon composite anode materials for lithium-ion battery, *J. Energy Chem.*, 2018, **27**(4), 1067–1090.

52 M. T. McDowell, S. W. Lee, J. T. Harris, B. A. Korgel, C. Wang, W. D. Nix and Y. Cui, In situ TEM of two-phase lithiation of amorphous silicon nanospheres, *Nano Lett.*, 2013, **13**(2), 758–764.

53 M. Li, D. Xue, Z. Rong, R. Fang, B. Wang, Y. Liang, X. Zhang, Q. Huang, Z. Wang, L. Zhu, L. Zhang, Y. Tang, S. Zhang and J. Huang, Stack Pressure Enhanced Size Threshold of Si Anode Fracture in All-Solid-State Batteries, *Adv. Funct. Mater.*, 2024, **35**(8), 2415696.

54 X. Liu, F. Fan, H. Yang, S. Zhang, J. Huang and T. Zhu, Self-Limiting Lithiation in Silicon Nanowires, *ACS Nano*, 2013, **7**(2), 1495–1503.

55 L. Ye, L. Yang, Y. Wang, J. Li and X. Li, Fast cycling of lithium metal in solid-state batteries by constriction-susceptible anode materials, *Nat. Mater.*, 2024, **23**(2), 244–251.

56 S. Imtiaz, I. S. Amiinu, D. Storan, N. Kapuria, H. Geaney, T. Kennedy and K. M. Ryan, Dense Silicon Nanowire Networks Grown on a Stainless-Steel Fiber Cloth: A Flexible and Robust Anode for Lithium-Ion Batteries, *Adv. Mater.*, 2021, **33**(52), e2105917.

57 H. Wu, G. Chan, J. W. Choi, I. Ryu, Y. Yao, M. T. McDowell, S. W. Lee, A. Jackson, Y. Yang, L. Hu and Y. Cui, Stable cycling of double-walled silicon nanotube battery anodes

through solid–electrolyte interphase control, *Nat. Nanotechnol.*, 2012, **7**(5), 310–315.

58 W. Wang, Z. Favors, R. Ionescu, R. Ye, H. H. Bay, M. Ozkan and C. S. Ozkan, Monodisperse Porous Silicon Spheres as Anode Materials for Lithium Ion Batteries, *Sci. Rep.*, 2015, **5**, 8781.

59 M. Yamamoto, M. Takatsu, R. Okuno, A. Kato and M. Takahashi, Nanoporous silicon fiber networks in a composite anode for all-solid-state batteries with superior cycling performance, *Sci. Rep.*, 2023, **13**(1), 17051.

60 D. H. Kim, S. H. Noh, Y.-C. Ha, D. G. Lee, J. T. Han, J. H. Choi and C. M. Park, Efficient Fabrication of High-Capacity Silicon Composite Anodes for All-Solid-State Lithium-Ion Batteries, *ACS Mater. Lett.*, 2025, **7**(4), 1211–1218.

61 M. Ling, Y. Xu, H. Zhao, X. Gu, J. Qiu, S. Li, M. Wu, X. Song, C. Yan, G. Liu and S. Zhang, Dual-functional gum arabic binder for silicon anodes in lithium ion batteries, *Nano Energy*, 2015, **12**, 178–185.

62 B. D. Polat and O. Keles, Improving Si Anode Performance by Forming Copper Capped Copper-Silicon Thin Film Anodes for Rechargeable Lithium Ion Batteries, *Electrochim. Acta*, 2015, **170**, 63–71.

63 H. T. Nguyen, F. Yao, M. R. Zamfir, C. Biswas, K. P. So, Y. H. Lee, S. M. Kim, S. N. Cha, J. M. Kim and D. Pribat, Highly Interconnected Si Nanowires for Improved Stability Li-Ion Battery Anodes, *Adv. Energy Mater.*, 2011, **1**(6), 1154–1161.

64 L. Cui, R. Ruffo, C. K. Chan, H. Peng and Y. Cui, Crystalline-Amorphous Core-Shell Silicon Nanowires for High Capacity and High Current Battery Electrodes, *Nano Lett.*, 2009, **9**(1), 491–495.

65 M.-H. Park, M. G. Kim, J. Joo, K. Kim, J. Kim, S. Ahn, Y. Cui and J. Cho, Silicon Nanotube Battery Anodes, *Nano Lett.*, 2009, **9**(11), 3844–3847.

66 Y. Yao, M. T. McDowell, I. Ryu, H. Wu, N. Liu, L. Hu, W. D. Nix and Y. Cui, Interconnected Silicon Hollow Nanospheres for Lithium-Ion Battery Anodes with Long Cycle Life, *Nano Lett.*, 2011, **11**(7), 2949–2954.

67 H. Kim, B. Han, J. Choo and J. Cho, Three-Dimensional Porous Silicon Particles for Use in High-Performance Lithium Secondary Batteries, *Angew. Chem., Int. Ed.*, 2008, **47**(52), 10151–10154.

68 S. Poetke, F. Hippauf, A. Baasner, S. Dörfler, H. Althues and S. Kaskel, Nanostructured Si–C Composites As High-Capacity Anode Material For All-Solid-State Lithium-Ion Batteries, *Batteries Supercaps*, 2021, **4**(8), 1323–1334.

69 Z. Zhang, Z. Sun, X. Han, Y. Liu, S. Pei, Y. Li, L. Luo, P. Su, C. Lan, Z. Zhang, S. Xu, S. Guo, W. Huang, S. Chen and M.-S. Wang, An all-electrochem-active silicon anode enabled by spontaneous Li–Si alloying for ultra-high performance solid-state batteries, *Energy Environ. Sci.*, 2024, **17**(3), 1061–1072.

70 J. Lee, D. Jin, J. Y. Kim, Y. Roh, H. Lee, S. H. Kang, J. Choi, T. Jo, Y. G. Lee and Y. M. Lee, Dry Pre-Lithiation for Graphite-Silicon Diffusion-Dependent Electrode for All-Solid-State Battery, *Adv. Energy Mater.*, 2023, **13**(25), 1–11.

71 L. Gu, J. Han, M. Chen, W. Zhou, X. Wang, M. Xu, H. Lin, H. Liu, H. Chen, J. Chen, Q. Zhang and X. Han, Enabling robust structural and interfacial stability of micron-Si anode toward high-performance liquid and solid-state lithium-ion batteries, *Energy Storage Mater.*, 2022, **52**, 547–561.

72 X. Han, M. Xu, L. Gu, C. Lan, M. Chen, J. Lu, B. Sheng, P. Wang, S. Chen and J. Chen, Monothetic and conductive network and mechanical stress releasing layer on micron-silicon anode enabling high-energy solid-state battery, *Rare Met.*, 2023, **43**, 1017–1029.

73 X. Zhang, D. Kong, X. Li and L. Zhi, Dimensionally Designed Carbon–Silicon Hybrids for Lithium Storage, *Adv. Funct. Mater.*, 2018, **29**(2), 1806061.

74 P. Niu, L. A. Arribas, M. Gich, C. F. Sánchez and A. Roig, Electrochemically Active Thin Carbon Films with Enhanced Adhesion to Silicon Substrates, *ACS Appl. Mater. Interfaces*, 2016, **8**(45), 31092–31099.

75 L. Zhao, J. C. Bennett, A. George and M. N. Obrovac, SiC-Free Carbon–Silicon Alloys Prepared by Delithiation as Lithium-Ion Battery Negative Electrodes, *Chem. Mater.*, 2019, **31**(11), 3883–3890.

76 Z. Yi, Y. Qian, C. Cao, N. Lin and Y. Qian, Porous Si/C microspheres decorated with stable outer carbon interphase and inner interpenetrated Si@C channels for enhanced lithium storage, *Carbon*, 2019, **149**, 664–671.

77 M. Ko, S. Chae, J. Ma, N. Kim, H. W. Lee, Y. Cui and J. Cho, Scalable synthesis of silicon-nanolayer-embedded graphite for high-energy lithium-ion batteries, *Nat. Energy*, 2016, **1**(9), 16113.

78 R. Zhou, H. Guo, Y. Yang, Z. Wang, X. Li and Y. Zhou, N-doped carbon layer derived from polydopamine to improve the electrochemical performance of spray-dried Si/graphite composite anode material for lithium ion batteries, *J. Alloys Compd.*, 2016, **689**, 130–137.

79 W. Yang, H. Ying, S. Zhang, R. Guo, J. Wang and W. Han, Electrochemical performance enhancement of porous Si lithium-ion battery anode by integrating with optimized carbonaceous materials, *Electrochim. Acta*, 2020, **337**, 135687.

80 J. Kim, C. Kim, I. Jang, J. Park, J. Kim, U. Paik and T. Song, Si nanoparticles embedded in carbon nanofiber sheathed with Li_6PS_5Cl as an anode material for all-solid-state batteries, *J. Power Sources*, 2021, **510**, 230425.

81 X. Han, W. Zhou, M. Chen, J. Chen, G. Wang, B. Liu, L. Luo, S. Chen, Q. Zhang, S. Shi and C. P. Wong, Interfacial nitrogen engineering of robust silicon/MXene anode toward high energy solid-state lithium-ion batteries, *J. Energy Chem.*, 2022, **67**, 727–735.

82 Y. Feng, H. Liu and Q. Lu, From non-carbon host toward carbon-free lithium-sulfur batteries, *Nano Res.*, 2023, **17**(3), 1337–1365.

83 M. Zhao, P. Wang, X. Bai, J. Liu, W. Feng and J. Li, Multifunctional composite binder with synergistic transport mechanism to achieve high performance all-solid-state batteries, *J. Power Sources*, 2023, **580**, 233350.

84 U. S. Vogl, P. K. Das, A. Z. Weber, M. Winter, R. Kostecki and S. F. Lux, Mechanism of interactions between CMC binder and Si single crystal facets, *Langmuir*, 2014, **30**(34), 10299–10307.

85 D. Qin, L. Xue, B. Du, J. Wang, F. Nie and L. Wen, Flexible fluorine containing ionic binders to mitigate the negative impact caused by the drastic volume fluctuation from silicon nano-particles in high capacity anodes of lithium-ion batteries, *J. Mater. Chem. A*, 2015, **3**(20), 10928–10934.

86 T. Yim, S. J. Choi, Y. N. Jo, T. H. Kim, K. J. Kim, G. Jeong and Y. J. Kim, Effect of binder properties on electrochemical performance for silicon-graphite anode: Method and application of binder screening, *Electrochim. Acta*, 2014, **136**, 112–120.

87 Q. Yuan, F. Zhao, Y. Zhao, Z. Liang and D. Yan, Reason analysis for Graphite-Si/SiO_x/C composite anode cycle fading and cycle improvement with PI binder, *J. Solid State Electrochem.*, 2014, **18**(8), 2167–2174.

88 E. A. Cave, T. A. Carr and C. W. Schlenker, Selective kinetic control of interfacial charge transfer reactions in Si-composite anodes for Li-ion batteries, *Energy Adv.*, 2024, **3**(9), 2186–2199.

89 W. Zhang, Q. Lu, G. Sun, Z. Chen, P. Yue, G. Zhang, B. Song and K. Song, Sodiophilic Interface Induces a NaF-Rich Solid Electrolyte Interface for Stable Sodium-Metal Batteries under Harsh Conditions, *Nano Lett.*, 2025, **25**(15), 6092–6100.

90 Z. Liu, S. Chen, Z. Shi, P. Qiu, K. He, Q. Lu, M. Yu and T. Liu, Multivalent Dipole Interactions-Driven Supramolecular Polymer Layer Enables Highly Stable Zn Anode Under Harsh Conditions, *Adv. Energy Mater.*, 2025, **15**(29), 2502010.

91 K. F. Chiu, S. H. Su, H. J. Leu and C. Y. Wu, Silicon thin film anodes coated on micron carbon-fiber current collectors for lithium ion batteries, *Surf. Coat. Technol.*, 2015, **267**, 70–74.

92 T. Hang, D. Mukoyama, H. Nara, T. Yokoshima, T. Momma, M. Li and T. Osaka, Electrochemical impedance analysis of electrodeposited Si–O–C composite thick film on Cu microcones-arrayed current collector for lithium ion battery anode, *J. Power Sources*, 2014, **256**, 226–232.

93 S. W. Kim, J. H. Yun, B. Son, Y.-G. Lee, K. M. Kim, Y. M. Lee and K. Y. Cho, Graphite/silicon hybrid electrodes using a 3D current collector for flexible batteries, *Adv. Mater.*, 2014, **26**(19), 2977–2982.

94 T. Jiang, S. Zhang, X. Qiu, W. Zhu and L. Chen, Preparation and characterization of silicon-based three-dimensional cellular anode for lithium ion battery, *Electrochem. Commun.*, 2007, **9**(5), 930–934.

95 Y. Tian, F. Ding, H. Zhong, C. Liu, Y.-B. He, J. Liu, X. Liu and Q. Xu, $Li_{6.75}La_3Zr_{1.75}Ta_{0.25}O_{12}$@amorphous Li_3OCl composite electrolyte for solid state lithium-metal batteries, *Energy Storage Mater.*, 2018, **14**, 49–57.

96 Y. Luo, J. Dong, Y. Wang, Z. Wang, Z. A. Chen and H. Zhang, Enhanced electrochemical performance of garnet $Li_7La_3Zr_2O_{12}$ electrolyte by efficient incorporation of LiCl, *Ceram. Int.*, 2024, **50**(23), 51055–51064.

97 M. Abreu-Sepúlveda, D. E. Williams, A. Huq, C. Dhital, Y. Li, M. P. Paranthaman, K. Zaghib and A. Manivannan, Synthesis and characterization of substituted garnet and perovskite-based lithium-ion conducting solid electrolytes, *Ionics*, 2015, **22**(3), 317–325.

98 S. Ohta, T. Kobayashi and T. Asaoka, High lithium ionic conductivity in the garnet-type oxide Li_{7-X} $La_3(Zr_{2-X}, Nb_X)$ O12 (X=0–2), *J. Power Sources*, 2011, **196**(6), 3342–3345.

99 S. Song, D. Sheptyakov, A. M. Korsunsky, H. M. Duong and L. Lu, High Li ion conductivity in a garnet-type solid electrolyte via unusual site occupation of the doping Ca ions, *Mater. Des.*, 2016, **93**, 232–237.

100 F. Ma, E. Zhao, S. Zhu, W. Yan, D. Sun, Y. Jin and C. Nan, Preparation and evaluation of high lithium ion conductivity $Li_{1.3}$ $Al_{0.3}Ti_{1.7}$ $(PO_4)_3$ solid electrolyte obtained using a new solution method, *Solid State Ionics*, 2016, **295**, 7–12.

101 Y. Chen, T. Wang, H. Chen, W. H. Kan, W. Yin, Z. Song, C. Wang, J. Ma, W. Luo and Y. Huang, Local structural features of medium-entropy garnet with ultra-long cycle life, *Matter*, 2023, **6**(5), 1530–1541.

102 S. M. Alizadeh, I. Moghim and M. Golmohammad, Synthesis and characterization of highly conductive Ga/Y co-doped LLZO by facile combustion sol-gel method, *Solid State Ionics*, 2023, **397**, 116260.

103 P. López-Aranguren, M. Reynaud, P. Głuchowski, A. Bustinza, M. Galceran, J. M. López del Amo, M. Armand and M. Casas-Cabanas, Crystalline LiPON as a Bulk-Type Solid Electrolyte, *ACS Energy Lett.*, 2021, **6**(2), 445–450.

104 S. Zhou, R. Tian, A. Wu, L. Lin and H. Huang, Fast Li^+ migration in LiPON electrolytes doped by multi-valent Fe ions, *J. Energy Chem.*, 2022, **75**(12), 349–359.

105 W. Huang, J. Li, K. Wei and L. Wang, Boosted Li^+ migration in LiPON electrolyte via introducing Ti-based bridge for solid-state thin film batteries, *J. Power Sources*, 2023, **587**, 233698.

106 P. Bron, S. Johansson, K. Zick, J. Schmedt auf der Günne, S. Dehnen and B. Roling, $Li_{10}SnP_2S_{12}$: An Affordable Lithium Superionic Conductor, *J. Am. Chem. Soc.*, 2013, **135**(42), 15694–15697.

107 Y. Kato, S. Hori, T. Saito, K. Suzuki, M. Hirayama, A. Mitsui, M. Yonemura, H. Iba and R. Kanno, High-power all-solid-state batteries using sulfide superionic conductors, *Nat. Energy*, 2016, **1**(4), 16030.

108 J. M. Whiteley, J. H. Woo, E. Hu, K.-W. Nam and S. H. Lee, Empowering the Lithium Metal Battery through a Silicon-Based Superionic Conductor, *J. Electrochem. Soc.*, 2014, **161**(12), A1812–A1817.

109 O. Kwon, M. Hirayama, K. Suzuki, Y. Kato, T. Saito, M. Yonemura, T. Kamiyama and R. Kanno, Synthesis, structure, and conduction mechanism of the lithium superionic conductor $Li_{10+\delta}Ge_{1+\delta}P_{2-\delta}S_{12}$, *J. Mater. Chem. A*, 2015, **3**(1), 438–446.

110 N. Kamaya, K. Homma, Y. Yamakawa, M. Hirayama, R. Kanno, M. Yonemura, T. Kamiyama, Y. Kato, S. Hama,

K. Kawamoto and A. Mitsui, A lithium superionic conductor, *Nat. Mater.*, 2011, **10**(9), 682–686.

111 Z. Liu, W. Fu, E. A. Payzant, X. Yu, Z. Wu, N. J. Dudney, J. Kiggans, K. Hong, A. J. Rondinone and C. Liang, Anomalous High Ionic Conductivity of Nanoporous β-Li_3PS_4, *J. Am. Chem. Soc.*, 2013, **135**(3), 975–978.

112 Z. Liu, F. Huang, J. Yang, B. Wang and J. Sun, New lithium ion conductor, thio-LISICON lithium zirconium sulfide system, *Solid State Ionics*, 2008, **179**(27–32), 1714–1716.

113 C. Dietrich, M. Sadowski, S. Sicolo, D. A. Weber, S. J. Sedlmaier, K. S. Weldert, S. Indris, K. Albe, J. Janek and W. G. Zeier, Local Structural Investigations, Defect Formation, and Ionic Conductivity of the Lithium Ionic Conductor $Li_4P_2S_6$, *Chem. Mater.*, 2016, **28**(23), 8764–8773.

114 Z. Jiang, H. Peng, Y. Liu, Z. Li, Y. Zhong, X. Wang, X. Xia, C. Gu and J. Tu, A Versatile $Li_{6.5}In_{0.25}P_{0.75}S_5I$ Sulfide Electrolyte Triggered by Ultimate-Energy Mechanical Alloying for All-Solid-State Lithium Metal Batteries, *Adv. Energy Mater.*, 2021, **11**(36), 2101521.

115 C. Yu, L. van Eijck, S. Ganapathy and M. Wagemaker, Synthesis, structure and electrochemical performance of the argyrodite Li_6PS_5Cl solid electrolyte for Li-ion solid state batteries, *Electrochim. Acta*, 2016, **215**, 93–99.

116 P. Hu, Y. Duan, D. Hu, B. Qin, J. Zhang, Q. Wang, Z. Liu, G. Cui and L. Chen, Rigid–Flexible Coupling High Ionic Conductivity Polymer Electrolyte for an Enhanced Performance of $LiMn_2O_4$/Graphite Battery at Elevated Temperature, *ACS Appl. Mater. Interfaces*, 2015, **7**(8), 4720–4727.

117 N. Wu, P.-H. Chien, Y. Li, A. Dolocan, H. Xu, B. Xu, N. S. Grundish, H. Jin, Y.-Y. Hu and J. B. Goodenough, Fast Li^+ Conduction Mechanism and Interfacial Chemistry of a NASICON/Polymer Composite Electrolyte, *J. Am. Chem. Soc.*, 2020, **142**(5), 2497–2505.

118 D. P. Nava, G. Guzmán, J. Vazquez Arenas, J. Cardoso, B. Gomez and I. Gonzalez, An experimental and theoretical correlation to account for the effect of $LiPF_6$ concentration on the ionic conductivity of poly(poly (ethylene glycol) methacrylate), *Solid State Ionics*, 2016, **290**, 98–107.

119 D. G. Hong, J. H. Baik, S. Kim and J. C. Lee, Solid polymer electrolytes based on polysiloxane with anion-trapping boron moieties for all-solid-state lithium metal batteries, *Polymer*, 2022, **240**, 124517.

120 J. Hu, W. Wang, B. Zhou, Y. Feng, X. Xie and Z. Xue, Poly(ethylene oxide)-based composite polymer electrolytes embedding with ionic bond modified nanoparticles for all-solid-state lithium-ion battery, *J. Membr. Sci.*, 2019, **575**, 200–208.

121 X. Yu, J. Li and A. Manthiram, Rational Design of a Laminated Dual-Polymer/Polymer–Ceramic Composite Electrolyte for High-Voltage All-Solid-State Lithium Batteries, *ACS Mater. Lett.*, 2020, **2**(4), 317–324.

122 H. Song, S. Xue, S. Chen, Z. Wang, Y. Song, J. Li, Z. Song, L. Yang and F. Pan, Polymeric Wetting Matrix for a Stable Interface between Solid-state Electrolytes and Li Metal Anode, *Chin. J. Struct. Chem.*, 2022, **41**(5), 1234–1245.

123 Z. Li, H. Huang, J. Zhu, J. Wu, H. Yang, L. Wei and X. Guo, Ionic Conduction in Composite Polymer Electrolytes: Case of PEO:Ga-LLZO Composites, *ACS Appl. Mater. Interfaces*, 2018, **11**(1), 784–791.

124 C. Zhao, X. Zhang, X. Cheng, R. Zhang, R. Xu, P. Chen, H. Peng, J. Huang and Q. Zhang, An anion-immobilized composite electrolyte for dendrite-free lithium metal anodes, *Proc. Natl. Acad. Sci. U. S. A.*, 2017, **114**(42), 11069–11074.

125 J. Bae, Y. Li, J. Zhang, X. Zhou, F. Zhao, Y. Shi, J. B. Goodenough and G. Yu, A 3D Nanostructured Hydrogel-Framework-Derived High-Performance Composite Polymer Lithium-Ion Electrolyte, *Angew. Chem., Int. Ed.*, 2018, **57**(8), 2096–2100.

126 J. Wan, J. Xie, X. Kong, Z. Liu, K. Liu, F. Shi, A. Pei, H. Chen, W. Chen, J. Chen, X. Zhang, L. Zong, J. Wang, L. Chen, J. Qin and Y. Cui, Ultrathin, flexible, solid polymer composite electrolyte enabled with aligned nanoporous host for lithium batteries, *Nat. Nanotechnol.*, 2019, **14**(7), 705–711.

127 R. Dong, J. Zheng, J. Yuan, Y. Li, T. Zhang, Y. Liu, Y. Liu, Y. Sun, B. Zhong, Y. Chen, Z. Wu and X. Guo, A polyethylene oxide/metal-organic framework composite solid electrolyte with uniform Li deposition and stability for lithium anode by immobilizing anions, *J. Colloid Interface Sci.*, 2022, **620**, 47–56.

128 S. J. Chiang, J. A. Kaduk and L. L. Shaw, High ionic conducting NaSICON enabled by mechanical activation enhanced reaction, *Mater. Chem. Phys.*, 2024, **312**, 128656.

129 J. Zhu, Y. Xiang, J. Zhao, H. Wang, Y. Li, B. Zheng, H. He, Z. Zhang, J. Huang and Y. Yang, Insights into the local structure, microstructure and ionic conductivity of silicon doped NASICON-type solid electrolyte $Li_{1.3}Al_{0.3}Ti_{1.7}P_3O_{12}$, *Energy Storage Mater.*, 2022, **44**, 190–196.

130 G. Kalita, T. Endo and T. Nishi, Recent development on low temperature synthesis of cubic-phase LLZO electrolyte particles for application in all-solid-state batteries, *J. Alloys Compd.*, 2023, **969**, 172282.

131 H. Sun, S. Kang and L. Cui, Prospects of LLZO type solid electrolyte: From material design to battery application, *Chem. Eng. J.*, 2023, **454**, 140375.

132 A. Karuthedath Parameswaran, S. Pazhaniswamy, L. Dekanovsky, N. Balakrishnan, C. S. Paneerselvam, M. V. Reddy, S. Adams and Z. Sofer, An integrated study on the ionic migration across the nano lithium lanthanum titanate (LLTO) and lithium iron phosphate-carbon (LFP-C) interface in all-solid-state Li-ion batteries, *J. Power Sources*, 2023, **565**, 232907.

133 X. Lu, M. Duan, J. Xiang, Y. Liang and S. Liu, Enhancement of ionic conductivity and fracture toughness by infiltrating porous $Li_{0.33}La_{0.56}TiO_3$ pellets, *J. Rare Earths*, 2024, **42**(2), 392–398.

134 W. Xia, Y. Zhao, F. Zhao, K. Adair, R. Zhao, S. Li, R. Zou, Y. Zhao and X. Sun, Antiperovskite Electrolytes for Solid-State Batteries, *Chem. Rev.*, 2022, **122**(3), 3763–3819.

135 R. Bayzou, J. Trébosc, A. K. Landry, R. B. Nuernberg, B. P. L. Cras, F. L. Cras, F. Pourpoint and O. Lafon,

Identification of phosphorus sites in amorphous LiPON thin film by observing internuclear proximities, *J. Magn. Reson.*, 2023, **354**, 107530.

136 K. Wang, L. Wei, L. Wang and K. Xu, Ab-initio investigation on the interface improvement by doping boron and carbon in $LiMn_2O_4$/LiPON all solid state battery, *J. Solid State Chem.*, 2022, **306**, 122797.

137 M. Inoue, H. Iwane, H. Kikuyama, Y. Tasaki, Y. Honda and T. Abe, Preparation of highly ionic conductive lithium phosphorus oxynitride electrolyte particles using the polygonal barrel-plasma treatment method, *J. Alloys Compd.*, 2022, **923**, 166350.

138 W. Ping, C. Yang, Y. Bao, C. Wang, H. Xie, E. Hitz, J. Cheng, T. Li and L. Hu, A silicon anode for garnet-based all-solid-state batteries: Interfaces and nanomechanics, *Energy Storage Mater.*, 2019, **21**, 246–252.

139 K. Marumoto, K. Nakano, Y. Kondo, M. Inaba and T. Doi, Tailored Design of a Nanoporous Structure Suitable for Thick Si Electrodes on a Stiff Oxide-Based Solid Electrolyte, *ACS Appl. Mater. Interfaces*, 2024, **16**(45), 62274–62281.

140 Y. Liang, H. Liu, G. Wang, C. Wang, Y. Ni, C. W. Nan and L. Z. Fan, Challenges, interface engineering, and processing strategies toward practical sulfide-based all-solid-state lithium batteries, *InfoMat*, 2022, **4**(5), 711–735.

141 Z. Zhang, L. Zhang, Y. Liu, X. Yan, B. Xu and L. Wang, One-step solution process toward formation of Li_6PS_5Cl argyrodite solid electrolyte for all-solid-state lithium-ion batteries, *J. Alloys Compd.*, 2020, **812**, 152103.

142 E. Gil González, L. Ye, Y. Wang, Z. Shadike, Z. Xu, E. Hu and X. Li, Synergistic effects of chlorine substitution in sulfide electrolyte solid state batteries, *Energy Storage Mater.*, 2022, **45**, 484–493.

143 S. Kaskel, H. Althues, S. Dörfler, A. Baasner, F. Hippauf and S. Poetke, Nanostructured Si—C Composites As High-Capacity Anode Material For All-Solid-State Lithium-Ion Batteries, *Batteries Supercaps*, 2021, **4**(8), 1323–1334.

144 D. Cao, X. Sun, Y. Li, A. Anderson, W. Lu and H. Zhu, Long-Cycling Sulfide-Based All-Solid-State Batteries Enabled by Electrochemo-Mechanically Stable Electrodes, *Adv. Mater.*, 2022, **34**(24), e2200401.

145 M. Grandjean, M. Pichardo, Y. Biecher, C. Haon and P. Chenevier, Matching silicon-based anodes with sulfide-based solid-state electrolytes for Li-ion batteries, *J. Power Sources*, 2023, **580**, 233386.

146 L. Fan, S. Wei, S. Li, Q. Li and Y. Lu, Recent Progress of the Solid-State Electrolytes for High-Energy Metal-Based Batteries, *Adv. Energy Mater.*, 2018, **8**(11), 1702657.

147 D. Zhou, D. Shanmukaraj, A. Tkacheva, M. Armand and G. Wang, Polymer Electrolytes for Lithium-Based Batteries: Advances and Prospects, *Chem*, 2019, **5**(9), 2326–2352.

148 Y. Wang, T. Li, X. Yang, Q. Yin, S. Wang, H. Zhang and X. Li, 2D Solid-Electrolyte Interphase Built by High-Concentration Polymer Electrolyte for Highly Reversible Silicon Anodes, *Adv. Energy Mater.*, 2023, **14**(2).

149 M. Lechartier, L. Porcarelli, H. Zhu, M. Forsyth, A. Guéguen, L. Castro and D. Mecerreyes, Single-ion polymer/LLZO hybrid electrolytes with high lithium conductivity, *Mater. Adv.*, 2022, **3**(2), 1139–1151.

150 E. M. Masoud, A. A. El-Bellihi, W. A. Bayoumy and M. A. Mousa, Organic–inorganic composite polymer electrolyte based on PEO–$LiClO_4$ and nano-Al_2O_3 filler for lithium polymer batteries: Dielectric and transport properties, *J. Alloys Compd.*, 2013, **575**, 223–228.

151 H. Huo, J. Sun, C. chen, X. Meng, M. He, N. Zhao and X. Guo, Flexible interfaces between Si anodes and composite electrolytes consisting of poly(propylene carbonates) and garnets for solid-state batteries, *J. Power Sources*, 2018, **383**, 150–156.

152 L. Zhang, Y. Lin, X. Peng, M. Wu and T. Zhao, A High-Capacity Polyethylene Oxide-Based All-Solid-State Battery Using a Metal–Organic Framework Hosted Silicon Anode, *ACS Appl. Mater. Interfaces*, 2022, **14**(21), 24798–24805.

153 X. Hu, W. Qiang and B. Huang, Preparation and properties of $Li_xLa_{0.5}TiO_3$ perovskite oxide electrolytes, *J. Am. Ceram. Soc.*, 2017, **100**(9), 4153–4158.

154 W. Xia, B. Xu, H. Duan, X. Tang, Y. Guo, H. Kang, H. Li and H. Liu, Reaction mechanisms of lithium garnet pellets in ambient air: The effect of humidity and CO_2, *J. Am. Ceram. Soc.*, 2017, **100**(7), 2832–2839.

155 Y. Zhang, J. Meng, K. Chen, H. Wu, J. Hu and C. Li, Garnet-Based Solid-State Lithium Fluoride Conversion Batteries Benefiting from Eutectic Interlayer of Superior Wettability, *ACS Energy Lett.*, 2020, **5**(4), 1167–1176.

156 M. Nose, A. Kato, A. Sakuda, A. Hayashi and M. Tatsumisago, Evaluation of mechanical properties of Na_2S–P_2S_5 sulfide glass electrolytes, *J. Mater. Chem. A*, 2015, **3**(44), 22061–22065.

157 X. Liu, Y. Peng, Q. Wang and L. Zhou, In-situ-interface-engineered mechanically robust solid polymer electrolyte for carbon fiber reinforced structural battery composites, *Compos. Sci. Technol.*, 2025, **270**, 111305.

158 J. Hou, W. Sun, Q. Yuan, L. Ding, Y. Wan, Z. Xiao, T. Zhu, X. Lei, J. Lin, R. Cheacharoen, Y. Zhou, S. Wang, F. Manshaii, J. Xie, W. Li and J. Zhao, Multiscale Engineered Bionic Solid-State Electrolytes Breaking the Stiffness-Damping Trade-Off, *Angew. Chem., Int. Ed.*, 2025, **64**(11), e202421427.